

© 2015 by Kevin Roberts. All rights reserved.

NUMERICAL STUDY OF P-WAVE  
SUPERCONDUCTIVITY IN SR<sub>2</sub>RO<sub>4</sub>

BY

KEVIN ROBERTS

DISSERTATION

Submitted in partial fulfillment of the requirements  
for the degree of Doctor of Philosophy in Physics  
in the Graduate College of the  
University of Illinois at Urbana-Champaign, 2015

Urbana, Illinois

Doctoral Committee:

Professor Anthony Leggett, Chair  
Professor Michael Stone, Director of Research  
Professor Alexey Bezryadin  
Professor Mats Selen

# Abstract

This thesis contains detailed numerical studies of the superconducting state of  $\text{Sr}_2\text{RuO}_4$ . This material's magnetic response displays  $hc/4e$  periodicity in multiply connected samples, a striking departure from  $hc/2e$  periodicity of the Little-Parks effect. One likely explanation for this is that, instead of the Cooper pairs existing in a spin-singlet state as in most conventional superconductors, the pairs form in an  $l = 1$ , or p-wave, angular momentum state. The additional spin degree of freedom offered by this angular momentum state allows the formation of half-quantum vortices possessing half of the usual flux quantum.

In Chapter 1, I briefly review p-wave superconductivity and see how it supports half-quantum vortices. In Chapter 2, I review the conventional Ginzburg-Landau formalism for treating superconductivity. We then extend this formalism to treat p-wave superconductivity. In Chapter 3, I discuss the numerical methods used to solve the coupled Ginzburg-Landau-Maxwell equations for the model. In Chapter 4, I present numerical solutions of the Ginzburg-Landau equations for the proposed model in realistic geometries and show that the data can be simulated using physically reasonable parameters. I also analyze an important alternative explanation to the presence of half-flux states involving integer vortices penetrating the walls of the sample. In Chapters 6 and 7, I present analyses of measurements of magnetoresistance oscillations in  $\text{Sr}_2\text{RuO}_4$  including evidence of phase-shift due to Abrikosov vortices.

*To my Mom and Dad.*

# Acknowledgements

This project would not have been possible without help and support from many people. Firstly, my adviser, Michael Stone, who taught me a lot of physics, revised many drafts of our publication, allowed me to explore on my own when possible, and prodded me when necessary. Special thanks goes to Raffi Budakian, upon whose experiments much of my work was based, and to my committee chair, Anthony Leggett, whose renowned expertise guided me through the tough spots when they arose. I would also like to thank my other committee member Mats Selen for his guidance and support through my entire graduate school experience.

I would like to thank former graduate students of the University of Illinois at Urbana-Champaign Department of Physics David Ferguson and Victor Vakaryuk for their valuable discussions and friendship. I probably learned more about superconductivity from them than everyone else combined. Thanks goes to my fiancé, Rachel Samanie, for helping to proofread the final draft of this thesis and her general good nature during the stresses of its completion. Finally, thanks to my family and friends for being so patient with me.

Financial support from National Science Foundation Grant No. DMR 09-03291 is gratefully acknowledged.

# Table of Contents

<b>List of Tables . . . . .</b>	<b>vi</b>
<b>List of Figures . . . . .</b>	<b>vii</b>
<b>1 Introduction . . . . .</b>	<b>1</b>
<b>2 Ginzburg-Landau Model . . . . .</b>	<b>5</b>
2.1 Ginzburg-Landau theory for s-wave superconductors . . . . .	5
2.1.1 De-dimensionalization . . . . .	6
2.1.2 Flux quantization . . . . .	9
2.2 Spin and charge stiffness . . . . .	10
2.3 Kinematic spin polarization . . . . .	13
2.4 Anisotropy . . . . .	14
2.5 Full model free energy and equations of motion . . . . .	16
<b>3 Numerical Method . . . . .</b>	<b>19</b>
3.1 Equations and boundary conditions . . . . .	19
<b>4 Results . . . . .</b>	<b>23</b>
4.1 Abrikosov Vortices . . . . .	25
<b>5 Vortex Energetics and Magnetoresistance Oscillations . . . . .</b>	<b>28</b>
5.1 Theory of Magnetoresistance Oscillations in Thin Rings . . . . .	30
5.1.1 The Little-Parks Effect . . . . .	30
5.1.2 Vortex-Induced Magnetoresistance Oscillations . . . . .	31
5.2 Oscillations in Superconducting Rings of $\text{Sr}_2\text{RuO}_4$ . . . . .	33
<b>6 Vortex Induced Phase Shifts . . . . .</b>	<b>37</b>
<b>7 Conclusions . . . . .</b>	<b>44</b>
<b>A Magnetization curves of ring-shaped superconductors . . . . .</b>	<b>46</b>
<b>B Magnetic moment curves of rings with weak links . . . . .</b>	<b>50</b>
<b>C Magnetic field delocalization and flux inversion . . . . .</b>	<b>58</b>
<b>D A Brief Introduction to the Finite-Element-Method . . . . .</b>	<b>62</b>
D.1 Weak formulation . . . . .	62
D.2 Discretization . . . . .	63
<b>References . . . . .</b>	<b>67</b>

# List of Tables

2.1	Table of the measured Ginzburg-Landau parameters of Sr <sub>2</sub> RuO <sub>4</sub> . . . . .	16
5.1	This table lists the mean width, $r_m$ , height, $h$ , width at the top, $w_{\text{top}}$ , width at the bottom, $w_{\text{bottom}}$ , median width $w_m$ , and their fitted values, given in nm, of the two samples analyzed in this thesis. The measured sample dimensions are accurate to within $\pm 10$ nm. . . . .	34
6.1	Measured Ginzburg-Landau parameters of NbSe <sub>2</sub> . The length scales are given in nanometers. . . . .	39
D.1	Linear shape functions for triangular mesh elements. . . . .	64

# List of Figures

1.1	SRO sample and magnetization curves showing integer flux transitions adapted from [1]. . . . .	1
1.2	Magnetization curves for various values of applied in-plane field. Adapted from [1]. The shaded region highlights the wedge-shaped character of the half-flux state's stability region. . . . .	2
2.1	A cartoon of the psuedopotential both above and below $T_c$ illustrating how Ginzburg-Landau theory captures the phenomenology of the phase-transition in superconductors. . . . .	6
2.2	Time series of vortices, having just entered the superconductor from the edges, move to form the triangular Abrikosov vortex lattice. . . . .	10
2.3	Time series of full-quantum vortices splitting into half-quantum vortices upon increase of the current-current coupling parameter. . . . .	12
2.4	The left-hand figures display $ \psi_\uparrow  +  \psi_\downarrow $ while the right-hand figures show only $ \psi_\downarrow $ . This time series shows how these components break apart to form the half-quantum vortices. . . . .	13
2.5	A unit cell of the layered perovskite structure of $\text{Sr}_2\text{RuO}_4$ . Ruthenium ions are red, strontium ions are blue, and oxygen ions are green. . . . .	15
3.1	Illustrating the unreliability of the field-cooled results. . . . .	21
3.2	Temperature plots of the phase in states with winding number $n=0$ , $n=1$ , and $n=2$ . . . . .	22
3.3	On the left is shown a representation of the simulated geometry. On the right is a top-down view of the simulated ring. The axes in both figures are labelled in units of $\lambda_{  }$ . . . . .	22
4.1	This figure shows an example of calculated relative free energies of the integer and half-flux states near the first transition. Each red line represents the free energy of the half-flux state at different values of applied in-plane magnetic field. Higher magnetic fields are seen to result in relatively lower free energies of the half-flux state. . . . .	23
4.2	Computed magnetization curves obtained using $\rho_{sp}/\rho_s = 0.25$ and a magnetic dipole moment of $0.55\mu_B$ . . . . .	24
4.3	The calculated in-plane spin magnetic moment for 200 Oe of applied in-plane field. . . . .	25
4.4	Slices through the sample plotting the magnitude of the order parameter. Darker areas indicate lower values of the order parameter while brighter regions indicate higher values. On the left is the sample penetrated by a vortex oriented in the x-direction. On the right is the sample without any Abrikosov vortices. . . . .	26

4.5	The free energies of a vortex oriented in the x-direction versus no vortex. . . . .	27
5.1	Magnetization curves for a sample with a diameter of $\approx 5\mu\text{m}$ . Adapted from [2]. . . . .	28
5.2	For a sample of smaller size, the suppression of the order-parameter near the edges has a more pronounced effect on the overall average magnitude and penetration depth. . . . .	29
5.3	The resultant change in resistance due to a shift in $T_c$ . . . . .	30
5.4	Data from [3]. The upper trace plots the applied magnetic field. . . . .	30
5.5	The experimental setup and data reported in [4]. The dotted line shows the resistance oscillations predicted by ???. Adapted from [4]. . . . .	31
5.6	SEM images and critical temperature measurements for the two sample rings analyzed in section ???. . . . .	33
5.7	CAD illustration of the samples used in [4]. . . . .	34
5.8	Fit of the magnetoresistance oscillations of Sample 1. . . . .	35
5.9	Fit of the magnetoresistance oscillations of Sample 2. . . . .	35
6.1	Plots of the potential barriers at various applied fields for two different ring widths. . . . .	37
6.2	Plot of the free energy of fluxoid states with and without an Abrikosov vortex penetrating the ring. . . . .	38
6.3	CAD drawing of Sample 1 sans-constrictions. . . . .	40
6.4	(a) SEM image of single-crystal $\text{NbSe}_2$ loop with median diameter $r \approx 160$ nm and width $w \approx 35$ nm. For measurements, the current is sourced from 1 to 6 and voltage is measured from 3 to 4. Scale bar is 100 nm. (b) SEM image of $\text{NbSe}_2$ loop with $r \approx 200$ nm and width $w \approx 70$ nm. The constricted regions have width $\approx 30$ nm. Here the current is sourced from 1 to 5 and voltage is measured from 3 to 6. Scale bar is 100 nm. (c) Magnetoresistance of loop in (a) at 4.2, 3.8, and 1.8 K (bottom to top) and 500 nA after subtracting of a monotonic background and offsetting curves for clarity. Vertical lines are separated by $H_0 = 840$ Oe. Shaded region denotes where phase shift occurs. (d) Magnetoresistance of loop in (b) at 1.8 K and 650 nA. Vertical lines are separated by $H_0 = 540$ Oe, except where indicated. Shaded regions denote where phase shifts are acquired. . . . .	42
6.5	Plot of the free energy of fluxoid states with and without an Abrikosov vortex penetrating the ring. . . . .	43
6.6	Figure (a) shows the measured resistance for various values of applied current. At higher applied currents the phase shift appears at lower applied magnetic fields. Figure (b) plots the field at which the Abrikosov vortex is presumed to enter versus applied current. . . . .	43
A.1	The free energy of a thin-walled cylinder for various values of the winding number of the order parameter. . . . .	47
A.2	The magnetic moment of a long, thin-walled cylinder. . . . .	48
A.3	The free energy curves of a two component system with current-current coupling. The states with half-integer flux winding are shown in red. . . . .	49
B.1	Thin ring Josephson junction with cylindrical symmetry. . . . .	51

B.2	Magnitude of the order parameter in junction with vortex. . . . .	51
B.3	Thin ring Josephson junction pinched in one direction. . . . .	52
B.4	Magnetization curves of a thin ring with a Josephson junction of varying coupling strengths. . . . .	53
B.5	Magnetization curves of 46 nm junction with in-plane field. . . . .	54
B.6	Magnetization curves of 46 nm junction with Meissner slope subtracted and curves offset . . . . .	54
B.7	Vortices in second geometry. . . . .	55
B.8	Magnetization curves of second ring. . . . .	56
B.9	Second ring with in-plane field rotated by 30 degrees. . . . .	57
C.1	From [5]. The behavior of the superfluid densities near the core of a vortex. On the left is plotted $ \psi_1 $ with $ \psi_2 $ on the right. The blue line represents a flux fraction of $5/6$ , the green, $5/7$ , and the red, $1/3$ . the component with the phase winding is $\psi_1$ . Notice the “W”-shape of the profile of $\psi_2$ . . . . .	60
C.2	Velocity profile of $\psi_\uparrow$ and $\psi_\downarrow$ in the half-flux state in a ring geometry. Contrary to integer flux states, the superfluid velocity of the component without a flux winding increases near the vortex core. . . . .	61
D.1	The mesh of a two-dimensional disk by triangles. (“Finite element triangulation” by Oleg Alexandrov - self-made, with en:Matlab. Licensed under Public Domain via Wikimedia Commons) . . . . .	64

# 1 Introduction

This thesis can be broadly divided into two parts based on the type of experiment under theoretical analysis. The unifying theme of these experiments is that they seek to probe the order-parameter of superconductors with exotic pairing. Superconductors with triplet  $p_x + ip_y$  pairing are interesting because they can host half-quantum vortices with Majorana core states and non-Abelian braid statistics [6, 7, 8]. There is indirect evidence that the layered superconductor  $\text{Sr}_2\text{RuO}_4$  has this pairing [9, 10, 11], and a search is on for “smoking gun” signatures that will confirm this. One signature — chiral edge currents — has proved elusive, but recent work [1] has found striking results suggesting that half-quantum vortices have been detected. If this result is correct, it strongly supports the spin triplet pairing character of the superconducting order parameter. Chapters 2 through 5 concern themselves with the construction and evaluation of a theoretical model seeking to explain this experiment’s results. Much of this material has been published in [12].

In the experiment reported in [1] a micron-sized annular flake of  $\text{Sr}_2\text{RuO}_4$  is mounted on a cantilever. Its magnetic moment is monitored as magnetic fields both perpendicular ( $B_x$ ) and parallel ( $B_z$ ) to the c-axis are applied. As  $B_z$  is increased, moment jumps corresponding to the entry of single-flux-quantum vortices into the hole in the annulus are easily observed (see figure 1.1).

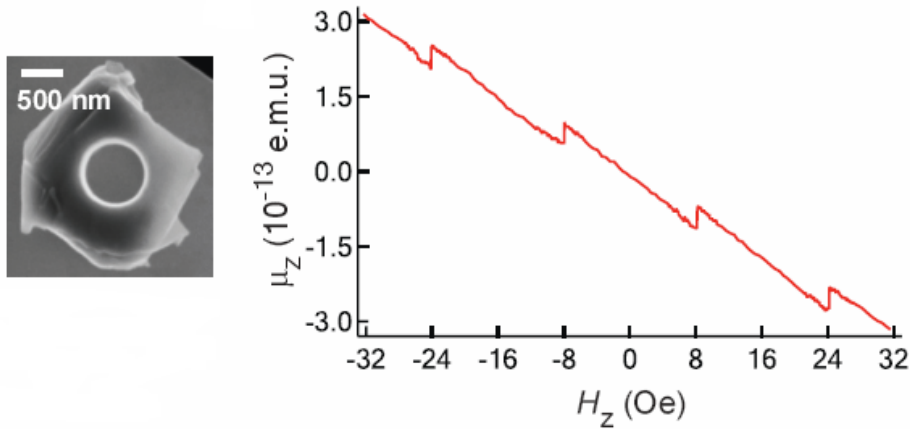


Figure 1.1: SRO sample and magnetization curves showing integer flux transitions adapted from [1].

When a sufficiently large in-plane field  $B_x$  is applied, these entry-event jumps break up into two separate events, each with one-half of the original magnetic-

moment jump. (See Figure 1.2.)

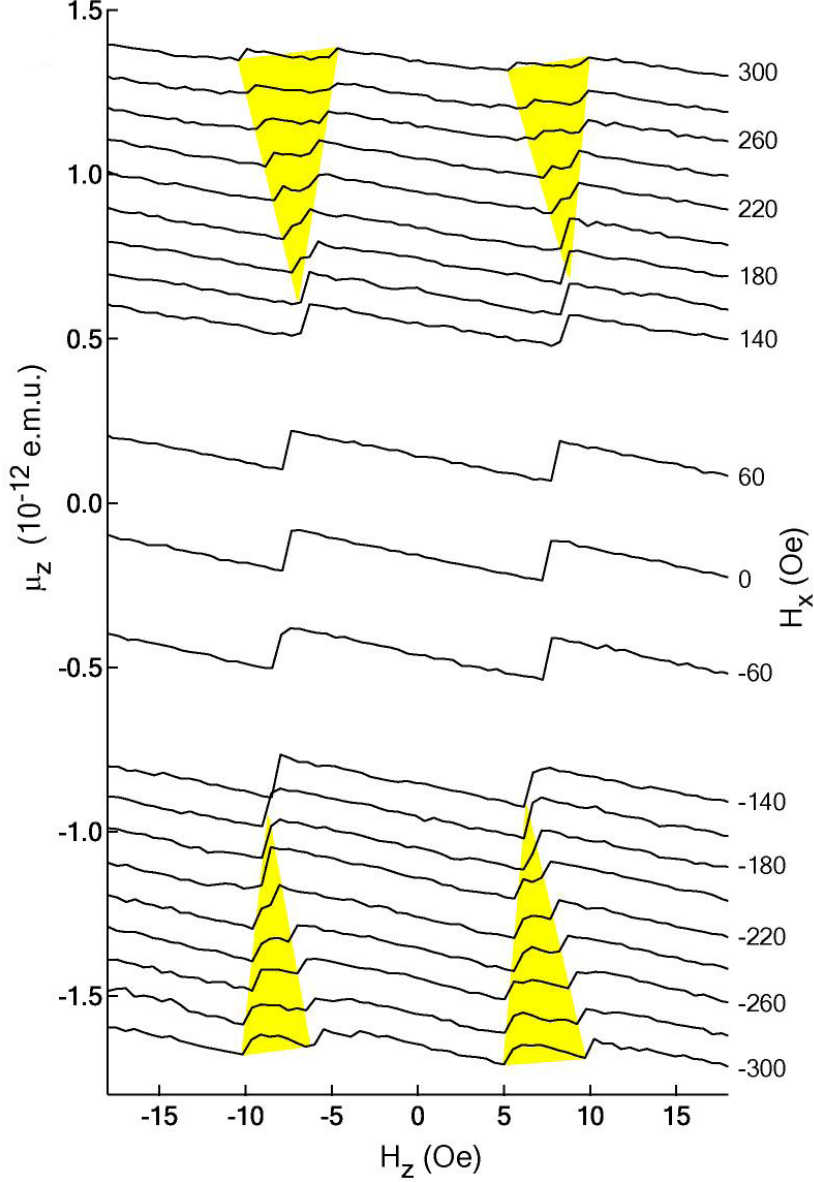


Figure 1.2: Magnetization curves for various values of applied in-plane field. Adapted from [1]. The shaded region highlights the wedge-shaped character of the half-flux state's stability region.

The most obvious explanation is that we are seeing half-quantum vortices: The large  $B$  field presumably has broken a spin orbit coupling that had held the spin-triplet order-parameter  $\mathbf{d}$  vector parallel to the pair angular momentum vector  $\mathbf{l}$ . The  $\mathbf{d}$  vector can now rotate freely in the  $x$ - $z$  plane and this freedom permits the existence of a half-quantum vortex defect around which the  $\mathbf{d}$  vector and the order-parameter phase  $\phi$  both rotate through an angle  $\pi$  while leaving the spin-triplet order parameter single valued. These rotations have the effect

of producing a phase-winding vortex in one spin component, while leaving the other with no phase winding. A circulating “anti-vortex” current is nonetheless induced in the second spin component by the magnetic field, and at large distances the spin-up and spin-down flow velocities become equal and opposite. This means that there is a long-range spin current surrounding the vortex. It is the necessity of reducing the logarithmically divergent free-energy-cost of this spin current that mandates the use of small annular samples [13].

As  $B_x$  is increased, the separation between the half-quantum jumps becomes larger. Vakaryuk and Leggett [14] have proposed that this phenomenon can be explained by a *kinematic spin polarization*. The different flow velocities for the up and down spin condensates give rise to an analogue of the Bernoulli effect which increases the magnitude of the order parameter for one condensate and decreases it for the other. The resulting magnetic polarization lies parallel to  $B_x$ , and so alters the energy cost for a vortex to enter the sample. Assessing whether or not the energy gain from Vakaryuk-Leggett mechanism is sufficient to explain the experimental data requires a detailed accounting of the energy in the three dimensional magnetic field surrounding the sample and in the degree of polarization of the condensate. In this thesis I perform this accounting by obtaining numerical solutions to an appropriate set of coupled Maxwell-Landau-Ginzburg-equations. With the specific geometry of the samples used in the experiment, and with reasonable values of the Landau-Ginzburg parameters, I find that I am able to qualitatively reproduce the experimental data.

Another scenario explaining the appearance of half steps in magnetization is one with bent Abrikosov vortices in a conventional, *s*-wave superconducting order parameter. By piercing the sidewall of the ring halfway between the top and bottom of the ring, bending, and then exiting the central hole, half of the ring will contain a flux winding and the ring will exhibit a half step of magnetization. However, I find that, because it is much smaller than the *c*-axis penetration depth, the ring is nearly transparent to the parallel field, and the lower critical field for vortices oriented in the *ab* plane to pierce the sample is much higher than the field at which half-flux states appear.

In chapters 6 and 7, I analyze magnetoresistance oscillations, periodic oscillations in the measured resistance as a function of applied magnetic field, of mesoscopic sized superconducting rings. The oscillations of  $\text{Sr}_2\text{RuO}_4$  measured in [4] are unconventional in the sense that their magnitude is an order of magnitude larger than what is predicted by the Little-Parks mechanism of the suppression of  $T_c$  by the magnetic field. A new theory of magnetoresistance oscillations has been proposed by Sochnikov et. al. [15] in which the oscillations in the resistance are caused by phase shifts in the order parameter from thermally activated vortices crossing the ring. In Chapter 6, I analyze the magnetoresistance oscillations in mesoscopic rings of  $\text{Sr}_2\text{RuO}_4$  in terms of this theory of thermally activated vortex resistance oscillations. I find that the theory is able to adequately describe the experimental data if one assumes a

drastic suppression in the magnitude of the order parameter in small samples of  $\text{Sr}_2\text{RuO}_4$ . This effect was also noticed in the data of [1]. At the present time, this is believed to be caused by scattering at the surface, averaging the gap over the Fermi surface. While the experiments of [4] were done without any applied magnetic field in the *ab*-plane and should not be expected to detect them, future experiments hope to detect the signature of half-quantum vortices by the presence of  $hc/4e$  periodicity in the magnetoresistance oscillations.

Experiments in magnetoresistance oscillations have also measured phase shifts in those oscillations, published examples of which can be found in [16]. In Chapter 7 I use the analytic London-limit solutions of Kogan, Clem, and Mints [17] and numerical calculations to show that these phase shifts are caused by the presence of Abrikosov vortices trapped in the bulk of the ring. I think that this could be a very exciting discovery. If phase shifts are shown to be a reliable detector of individual vortices, it would provide a powerful new tool for studying vortex dynamics.

# 2 Ginzburg-Landau Model

## 2.1 Ginzburg-Landau theory for s-wave superconductors

In order to understand the model used in this work, it is helpful to review standard Ginzburg-Landau theory and its generalization to superconductors exhibiting exotic pairing.

The Ginzburg-Landau model for s-wave superconductors is embodied in the Ginzburg-Landau free energy[18, Chapter 4]

$$F[\psi, \psi^*, \mathbf{A}] = \int_{\Omega} d^3x \left\{ \frac{\hbar^2}{2m} \left| \left( \nabla - \frac{2ie}{\hbar} \mathbf{A} \right) \psi \right|^2 + \alpha |\psi|^2 + \frac{\beta}{2} |\psi|^4 + \frac{1}{2\mu_0} |\nabla \times \mathbf{A} - \mathbf{B}_{\text{ext}}|^2 \right\} \quad (2.1)$$

where  $\psi$  represents the complex scalar order-parameter. In this case, it can be taken to be the center-of-mass wave-function of the s-wave Cooper-pairs. Here,  $\hbar$  is the reduced Planck's constant,  $e$  the charge of the electron,  $m$  a phenomenological mass (not the electron's mass), and  $\alpha$  and  $\beta$  are temperature dependent parameters.

Minimizing this free energy with respect to  $\psi^*$  (see [19, Chapter 1] for this procedure) gives the Ginzburg-Landau equations

$$-\frac{\hbar^2}{2m} \left( \nabla - \frac{2ie}{\hbar} \mathbf{A} \right)^2 \psi + \alpha \psi + \beta |\psi|^2 \psi = 0 \text{ in } \Omega \quad (2.2)$$

$$\frac{1}{\mu_0} \nabla \times (\nabla \times \mathbf{A} - \mathbf{B}_{\text{ext}}) - 2e \mathbf{J} = 0 \text{ in } \Omega \quad (2.3)$$

where

$$\mathbf{J} = \frac{\hbar}{2mi} \left\{ \psi^* \left( \nabla - \frac{2ie}{\hbar} \mathbf{A} \right) \psi - \psi \left( \nabla + \frac{2ie}{\hbar} \mathbf{A} \right) \psi^* \right\} \quad (2.4)$$

is the Cooper-pair number current, along with the boundary conditions

$$\mathbf{n} \cdot \left( \nabla - \frac{2ie}{\hbar} \mathbf{A} \right) \psi = 0 \text{ on } \partial\Omega \quad (2.5)$$

and

$$\nabla \times (\nabla \times \mathbf{A} - \mathbf{B}_{\text{ext}}) = 0. \quad (2.6)$$

Now consider a homogeneous superconductor in the absence of applied magnetic fields. Setting  $\mathbf{A} = 0$ , the free energy reduces to

$$f = \alpha(T)|\psi|^2 + \beta(T)|\psi|^4 \quad (2.7)$$

and is sometimes referred to as the psuedopotential. Here I have indicated the temperature dependence of  $\alpha$  and  $\beta$  explicitly. Ginzburg-Landau theory captures the phenomenology of the superconducting phase transition by allowing  $\alpha$  to change sign at a critical temperature  $T_c$ . At  $T > T_c$ ,  $\alpha > 0$  and the minimum of the free energy is obtained by taking  $|\psi| = 0$ . Below  $T_c$ ,  $\alpha$  becomes negative and the free energy is minimized by

$$\psi_0 \equiv \frac{|\alpha|}{\beta}. \quad (2.8)$$

More precisely, any order-parameter differing by a phase from  $\psi_0$  would minimize the free-energy.

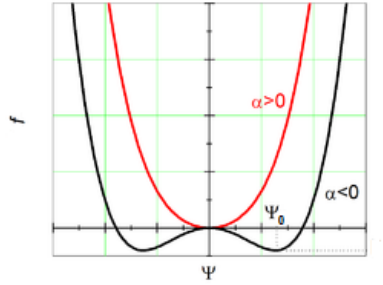


Figure 2.1: A cartoon of the psuedopotential both above and below  $T_c$  illustrating how Ginzburg-Landau theory captures the phenomenology of the phase-transition in superconductors.

### 2.1.1 De-dimensionalization

Some dimensional analysis reveals two important length-scales in Ginzburg-Landau theory. The units of the free energy, equation (2.1), must clearly be Joules,  $[F] = \text{J}$ . Since

$$\left[ d^3x \frac{\hbar^2}{2m} \nabla^2 \right] = \text{m}^3 \frac{\text{J}^2 \text{s}^2}{\text{kg}} \text{m}^{-2} = \frac{\text{J}^2 \text{s}^2 \text{m}}{\text{kg}}, \quad (2.9)$$

the units of the order-parameter must be  $[\psi] = \text{m}^{-3/2}$ . This means that the units of  $\alpha$  must be Joules,  $\text{J}$ .

Now examine equation (2.2) for the case of vanishing vector potential but

non-zero gradients in  $\psi$ ,

$$-\frac{\hbar^2}{2m}\nabla^2\psi + \alpha\psi + \beta|\psi|^2\psi = 0. \quad (2.10)$$

Dividing this equation by  $\alpha$  we have

$$-\frac{\hbar^2}{2m\alpha}\nabla^2\psi + \psi + \frac{\beta}{\alpha}|\psi|^2\psi = 0. \quad (2.11)$$

The combination  $(\hbar^2/2m\alpha)\nabla^2$  is clearly dimensionless. This shows that

$$\xi \equiv \sqrt{\frac{\hbar^2}{2m|\alpha|}} \quad (2.12)$$

is the natural length-scale for variations in the order-parameter and is referred to as the coherence length.

A similar calculation reveals the natural length-scale for variations in the vector potential. Let's consider equations (2.3) and (2.4) with a vanishing applied field,  $\mathbf{B}_{\text{ext}} = 0$ , and vanishing gradients in  $\psi$ . We then have

$$\frac{1}{\mu_0}\nabla \times \nabla \times \mathbf{A} + \frac{4e^2}{m}|\psi|^2\mathbf{A} = 0. \quad (2.13)$$

Now, using the identity  $\nabla \times \nabla \times \mathbf{A} = \nabla(\nabla \cdot \mathbf{A}) - \nabla^2\mathbf{A}$ , assuming the Coulomb gauge,  $\nabla \cdot \mathbf{A} = 0$ , and dividing by  $4e^2/m|\psi|^2$ , we arrive at

$$\frac{m}{4e^2\mu_0|\psi|^2}\nabla^2\mathbf{A} - \mathbf{A} = 0. \quad (2.14)$$

We see that

$$\lambda \equiv \sqrt{\frac{m}{4e^2\mu_0|\psi|^2}} \quad (2.15)$$

describes the natural length-scale for gradients in  $\mathbf{A}$  and is referred to as the penetration depth.

The ratio of the penetration depth and correlation length,

$$\kappa = \frac{\lambda}{\xi} \quad (2.16)$$

is called the Ginzburg-Landau parameter. Superconductors for which  $\kappa < 1/\sqrt{2}$  are called Type I, while those with  $\kappa > 1/\sqrt{2}$  are called Type II. The phenomenological difference between these two types are vast and rich and a complete discussion is the scope of this thesis. However, I will mention here that Type II superconductors are those that exhibit vortices in the presence of magnetic fields. All of the superconducting materials I discuss are Type II.

Now imagine a situation in which the order-parameter is at its equilibrium value,  $\sqrt{|\alpha|/\beta}$ , and the superconductor is in a perfect Meissner state,  $\mathbf{A} = 0$ .

Then, setting the free energy density equal to zero gives

$$\alpha \frac{|\alpha|}{\beta} + \frac{\beta}{2} \frac{|\alpha|^2}{\beta^2} + \frac{1}{2\mu_0} |\mathbf{B}_{\text{ext}}|^2 = 0 \quad (2.17)$$

which defines the thermodynamic critical field

$$B_c = \sqrt{\frac{\mu_0 |\alpha|^2}{\beta}}. \quad (2.18)$$

This is the field at which the free energy cost of expelling the magnetic field from the bulk of the superconductor equals the free energy gained by being in the superconducting state.

By defining  $\psi \equiv \psi_0 \tilde{\psi}$ ,  $\mathbf{x} = \lambda \tilde{\mathbf{x}}$ , and  $\mathbf{A} \equiv \sqrt{2} B_c \lambda \tilde{\mathbf{A}}$ , I can use these results to write a dimensionless free-energy suitable for numerical work,

$$\tilde{F}[\tilde{\psi}, \tilde{\psi}^*, \tilde{\mathbf{A}}] = \int_{\Omega} d^3 \tilde{x} \left\{ \left| \left( \frac{\nabla}{\kappa} - i \tilde{\mathbf{A}} \right) \tilde{\psi} \right|^2 + \text{sgn}(\alpha) |\tilde{\psi}|^2 + \frac{1}{2} |\tilde{\psi}|^4 + |\nabla \times \tilde{\mathbf{A}} - \tilde{\mathbf{B}}_{\text{ext}}|^2 \right\}, \quad (2.19)$$

which gives the free energy in units of  $\lambda^2 |\alpha|^2 / \beta$ .

There are some useful things to keep in mind when working in these dimensionless units. For instance, notice that the only parameter that explicitly enters the free energy is the Ginzburg-Landau parameter,  $\kappa$ , the ratio of  $\lambda$  and  $\xi$ . However, in order to determine the correct geometric parameters, you must know  $\lambda$  separately, since lengths are measured in penetration depths.

One also needs to know how to translate quantities back into dimensionful units, and vice-versa. Knowing how to do so can save valuable calculation time. For instance, suppose I want to study the periodicity of a thin ring. I know that the size of a period is given by  $\pi r^2 B_{\text{ext}} = \Phi_0$ . What value of  $\tilde{\mathbf{B}}$  does this correspond to? Firstly, since we are going to have to translate the distances into units of penetration depths, write  $r = \gamma \lambda$ . We also know that  $\mathbf{B} = \sqrt{2} B_c \tilde{\mathbf{B}}$ . Using these in the above expression we have

$$\sqrt{2} \pi \gamma^2 \lambda^2 B_c \tilde{B} = \Phi_0. \quad (2.20)$$

This expression would seem to indicate that by varying the critical field  $B_c$  while keeping  $\lambda$  fixed, we could vary the periodicity of the ring. This is contrary to experience as the periodicity of superconducting rings is usually insensitive to the critical field. Since  $\kappa$  is the only parameter to explicitly enter the dimensionless equations of motion,  $B$  must depend only on  $\kappa$  and the geometry parameter  $\gamma$ . The reason some of these expressions look strange is that in order to be internally consistent, Ginzburg-Landau theory fixes the thermodynamic critical field if  $\lambda$  and  $\xi$  are known and they may be swapped for one another.

Tinkham[18, Eq. 4.27] gives the expression

$$\kappa\Phi_0 = 2\sqrt{2}\pi\lambda^2 B_c. \quad (2.21)$$

Combining this with the previous expression for  $\Phi_0$  gives  $\tilde{B} = 2/\gamma^2\kappa$  as the periodicity of a thin ring in dimensionless units. Multiplying by  $\sqrt{2}B_c$  and using Tinkham's equation, this reduces to

$$B = \frac{\Phi_0}{\pi\gamma^2\lambda^2} = \frac{\Phi_0}{\pi r^2} \quad (2.22)$$

as expected.

### 2.1.2 Flux quantization

Consider the number-current, equation (2.4). If we write  $\psi$  as  $|\psi|e^{i\theta}$ , this expression reduces to

$$\mathbf{J} = \frac{\hbar}{m}|\psi|^2 \left( \nabla\theta - \frac{2e}{\hbar}\mathbf{A} \right) \equiv |\psi|^2 \mathbf{v}_s \quad (2.23)$$

which defines the supercurrent velocity  $\mathbf{v}_s$ . Rearranging this expression and integrating around a closed path we can write

$$\frac{\hbar}{2e} \oint \nabla\theta \cdot d\mathbf{l} = \Phi + 2e\mu_0 \oint \lambda^2 \mathbf{J} \cdot d\mathbf{l}. \quad (2.24)$$

where  $\Phi = \oint \mathbf{A} \cdot d\mathbf{l}$  is the flux threading the closed path. The expression on the left is called the fluxoid,  $\Phi'$ . Because of the single valuedness of the order-parameter, it must be quantized to multiples of  $h/2e \equiv \Phi_0$ , the magnetic flux quantum. If we suppose that the closed path taken is deep enough in the interior of a superconductor that we may ignore the current  $\mathbf{J}$ , the expression reduces to

$$\Phi = n\Phi_0, \quad (2.25)$$

showing that the magnetic flux piercing a superconductor is quantized. This result should be contrasted with those of the next section in which I show how flux may be quantized in units half as large in superconductors that admit p-wave pairing.

In Type II superconductors, which support the presence of vortices, it is energetically favorable for each vortex to contain only one quantum of flux. The vortices possess complex interactions, forming the so-called Abrikosov vortex lattice, as shown in Figure 2.2. These interactions are one of the primary motivations in choosing the ring-like geometry of [1]. Once the vortices enter the hole in interior of the ring, the interactions are no longer of any consideration simply because there are no more vortices. The energetics of the resulting ladder of fluxoid states is much easier to study. An introduction to the energetics of

these fluxoid states and the resulting magnetization curves is given in Appendix A.

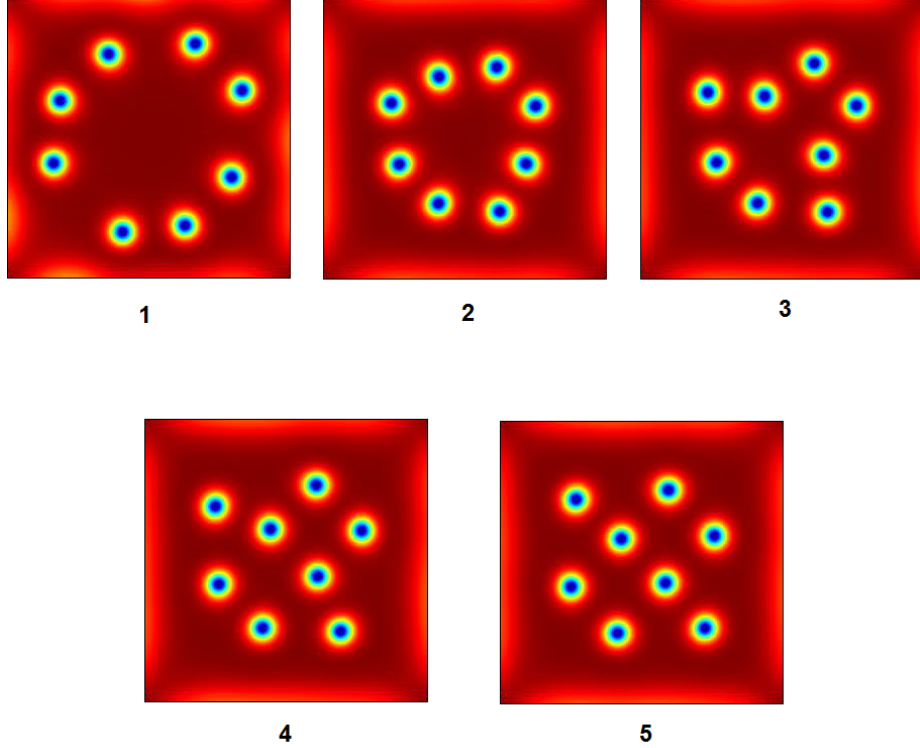


Figure 2.2: Time series of vortices, having just entered the superconductor from the edges, move to form the triangular Abrikosov vortex lattice.

## 2.2 Spin and charge stiffness

For a spin-triplet  $p_x+ip_y$  superconductor with a fixed orbital angular momentum vector  $\mathbf{l} = \hat{\mathbf{z}}$ , the order parameter is matrix-valued and of the form[20, 11, 21]

$$\begin{bmatrix} \Delta_{\uparrow\uparrow} & \Delta_{\uparrow\downarrow} \\ \Delta_{\downarrow\uparrow} & \Delta_{\downarrow\downarrow} \end{bmatrix} = |\Delta| e^{i\chi} (-i\sigma_2 \boldsymbol{\sigma} \cdot \mathbf{d}) = |\Delta| e^{i\chi} \begin{bmatrix} -(d_1 + id_2) & d_3 \\ d_3 & d_1 - id_2 \end{bmatrix}. \quad (2.26)$$

The  $\mathbf{d}$  vector has unit length, and for our application we will assume that it is perpendicular to a spin-quantization axis  $\mathbf{e}_3$ , which need not be the  $z$  axis. We therefore set  $d_3 = 0$ ,  $d_1 + id_2 = e^{i\phi}$ , and define the phases of  $\Delta_{\uparrow\uparrow}$  and  $\Delta_{\downarrow\downarrow}$  to be  $\theta_\uparrow + \pi$  and  $\theta_\downarrow$  respectively. Then

$$\chi = \frac{1}{2}(\theta_\uparrow + \theta_\downarrow), \quad (2.27)$$

$$\phi = \frac{1}{2}(\theta_\uparrow - \theta_\downarrow). \quad (2.28)$$

The authors of [13] (see also [22, 23]) write the free-energy density in the London form

$$K_{\text{London}} = \rho_s \left| \nabla \chi - \frac{2e}{\hbar} \mathbf{A} \right|^2 + \rho_{\text{spin}} |\nabla \phi|^2. \quad (2.29)$$

This expression contains only the Goldstone fields  $\chi$  and  $\phi$  and so ignores the free-energy cost of gradients in the magnitude of the order parameter. Nonetheless Eq. (2.29) captures the essential far-from-core vortex energetics. In particular, in a half-quantum vortex either  $\theta_\uparrow$  or  $\theta_\downarrow$  (but not both) rotate through  $\pm 2\pi$ . Then  $\chi$  and  $\phi$  rotate through  $\pm\pi$ . Far from the vortex core, the  $\mathbf{B}$  field will adjust so as to make the first term in  $K$  zero, hence the total flux threading the half-vortex is given by

$$\Phi_{1/2} = \oint \mathbf{A} \cdot d\mathbf{r} = \frac{\hbar}{2e} \oint \nabla \chi \cdot d\mathbf{r} = \frac{1}{4} \left( \frac{2\pi\hbar}{e} \right) = \frac{1}{2} \Phi_0. \quad (2.30)$$

The remaining term *cannot* be screened by the  $\mathbf{B}$  field and gives a contribution to the vortex energy that is logarithmically divergent at large distances. This divergent energy cost means that a half-quantum vortex will be disfavoured unless the spin stiffness  $\rho_{\text{spin}}$  is small and a finite size to the superconducting region cuts-off the long-distance contribution.

The angle-valued Goldstone fields are not suitable for numerical work as they are not singled-valued in the presence of vortices. We need to write the free energy in terms of single-valued fields. We therefore introduce fields  $\psi_\uparrow = |\psi_\uparrow| \exp\{i\theta_\uparrow\}$  and  $\psi_\downarrow = |\psi_\downarrow| \exp\{i\theta_\downarrow\}$ . The simplest form for the Landau-Ginzburg free-energy density that has the correct symmetries contains the kinetic-energy density

$$K_{\text{Landau}} = \frac{\hbar^2}{2m^*} \left\{ \left| \left( \nabla - \frac{2ie}{\hbar} \mathbf{A} \right) \psi_\uparrow \right|^2 + \left| \left( \nabla - \frac{2ie}{\hbar} \mathbf{A} \right) \psi_\downarrow \right|^2 + 2b \mathbf{J}_\uparrow \cdot \mathbf{J}_\downarrow \right\}, \quad (2.31)$$

where

$$\mathbf{J}_\uparrow = \frac{ie\hbar}{m^*} \left( \psi_\uparrow^* \left( \nabla - \frac{2ie}{\hbar} \mathbf{A} \right) \psi_\uparrow - \psi_\uparrow \left( \nabla + \frac{2ie}{\hbar} \mathbf{A} \right) \psi_\uparrow^* \right), \quad (2.32)$$

$$\mathbf{J}_\downarrow = \frac{ie\hbar}{m^*} \left( \psi_\downarrow^* \left( \nabla - \frac{2ie}{\hbar} \mathbf{A} \right) \psi_\downarrow - \psi_\downarrow \left( \nabla + \frac{2ie}{\hbar} \mathbf{A} \right) \psi_\downarrow^* \right). \quad (2.33)$$

The current-current interaction introduces no new magnitude-gradient free-energy cost, and so does not affect the coherence length.

If we set  $\psi_\uparrow = |\psi| e^{i\theta_\uparrow}$ , etc., and temporarily ignore derivatives of the common

magnitude  $|\psi|$ , then

$$\begin{aligned} K_{\text{landau}} &\approx |\psi|^2 \frac{\hbar^2}{2m^*} \left\{ \left| \nabla \theta_\uparrow - \frac{2e}{\hbar} \mathbf{A} \right|^2 + \left| \nabla \theta_\downarrow - \frac{2e}{\hbar} \mathbf{A} \right|^2 \right. \\ &\quad \left. + 2b \left( \nabla \theta_\uparrow - \frac{2e}{\hbar} \mathbf{A} \right) \cdot \left( \nabla \theta_\downarrow - \frac{2e}{\hbar} \mathbf{A} \right) \right\} \\ &= |\psi|^2 \frac{\hbar^2}{2m^*} \left\{ 2(1+b) \left| \nabla \chi - \frac{2e}{\hbar} \mathbf{A} \right|^2 + 2(1-b) |\nabla \phi|^2 \right\}, \end{aligned} \quad (2.34)$$

which is to be compared with desired London form of [13]. As  $\rho_{\text{spin}}$  must be positive,  $b$  must be less than unity. Being just less than unity encourages half-quantum vortices.

The presence of the term  $2b \mathbf{J}_\uparrow \cdot \mathbf{J}_\downarrow$  in the free energy density alters the current  $\mathbf{J}_{\text{maxwell}}$  that couples to the magnetic field. We have

$$\mathbf{J}_{\text{maxwell}} = \mathbf{J}_\uparrow + \mathbf{J}_\downarrow - \frac{8e^2 b}{m^*} (|\psi_\uparrow|^2 \mathbf{J}_\downarrow + |\psi_\downarrow|^2 \mathbf{J}_\uparrow). \quad (2.35)$$

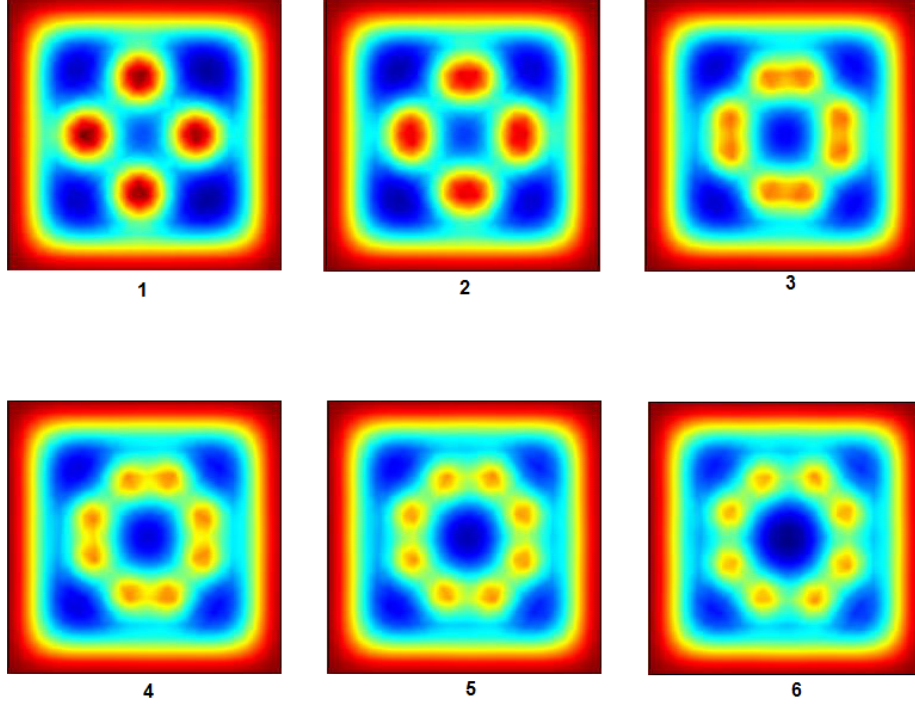


Figure 2.3: Time series of full-quantum vortices splitting into half-quantum vortices upon increase of the current-current coupling parameter.

The effect of the current-current interaction can be seen most starkly in figure 2.3. The frames in figure 2.3 show temperature plots of the magnetic field in a two-dimensional slab of superconducting material with kinetic energy density given by equation (2.31). In frame 1, the coupling parameter  $b$  is equal

to zero and the sample is penetrated by four vortices each containing a full quantum of flux. The coupling parameter  $b$  is then increased linearly with time. When  $b$  reaches the geometry dependent critical value, each of these vortices splits into two separate vortices, each containing half of the original flux quantum as evidenced by a darker shade in the temperature plot.

Another interesting figure that gives more insight into what's going on is figure 2.4. The left-hand plot of the time series shows temperature plots of  $|\psi_\uparrow| + |\psi_\downarrow|$  while the right-hand figures show only  $|\psi_\downarrow|$ . This shows that the  $\psi_\downarrow$  component, itself, is what forms one set of the half-quantum vortices,  $\psi_\uparrow$  the other. One can think of the current-current coupling term in equation (2.31) as imposing an energy cost for the vortices of  $\psi_\uparrow$  and  $\psi_\downarrow$  to exist in the same space. The components then separate from each other to form the half-quantum vortices.

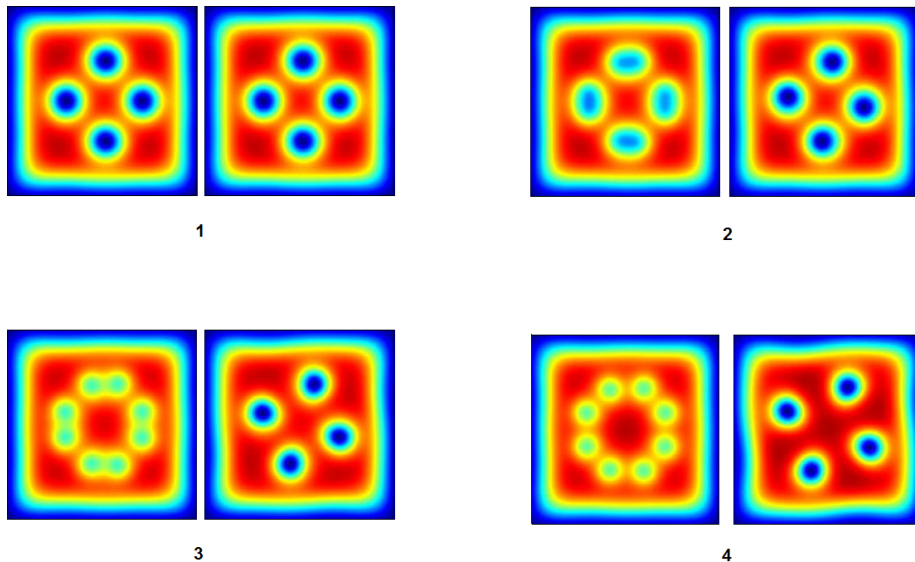


Figure 2.4: The left-hand figures display  $|\psi_\uparrow| + |\psi_\downarrow|$  while the right-hand figures show only  $|\psi_\downarrow|$ . This time series shows how these components break apart to form the half-quantum vortices.

## 2.3 Kinematic spin polarization

Legget and Vakaryuk propose [14] that the dependence of the half-quantum vortex stability region on the applied in-plane field  $B_x$  can be understood via the existence of a spontaneous spin polarization in the half-quantum vortex state that arises from the difference between the spin-up and spin-down condensate velocities  $\mathbf{v}_\uparrow$  and  $\mathbf{v}_\downarrow$  in the half-quantum vortex.

The polarization occurs because for each of the two spin components in the

Landau-Ginzburg theory we have a version of Bernoulli's equation:

$$\frac{1}{2}m^*|\mathbf{v}_{\uparrow,\downarrow}|^2 + \frac{\partial u}{\partial \rho_{\uparrow,\downarrow}} = \text{const.} \quad (2.36)$$

Here  $\rho_{\uparrow,\downarrow} = |\psi_{\uparrow,\downarrow}|^2$ , and

$$u(\rho) = \alpha\rho + \frac{1}{2}\beta\rho^2, \quad (2.37)$$

is the potential part of the Landau-Ginzburg free energy density.

As a consequence, as the superflow becomes faster, the order-parameter density lowers. The polarizing tendency is proportional to

$$|\mathbf{v}_\uparrow|^2 - |\mathbf{v}_\downarrow|^2 = (\mathbf{v}_\uparrow + \mathbf{v}_\downarrow) \cdot (\mathbf{v}_\uparrow - \mathbf{v}_\downarrow) \quad (2.38)$$

$$= \mathbf{v}_{\text{charge}} \cdot \mathbf{v}_{\text{spin}} \quad (2.39)$$

This polarizing tendency gives rise to spin magnetic moment

$$\boldsymbol{\mu}_{\text{spin}} = g\mu_B (|\psi_\uparrow|^2 - |\psi_\downarrow|^2) \mathbf{e}_3 \quad (2.40)$$

Here  $\mu_B$  denotes the Bohr magneton, and  $g$  is a phenomenological parameter that we expect to be of order unity. (If  $|\psi|_{\uparrow,\downarrow}^2$  were the actual density of cooper pairs, and if each of the two electrons in the pair contributes a Dirac moment of  $\mu_{\text{electron}} \approx \mu_B$ , we would have  $g = 2$ .) The induced moment couples to the magnetic field to give a free-energy contribution

$$\Delta F = -\mathbf{B} \cdot \boldsymbol{\mu}_{\text{spin}}. \quad (2.41)$$

Jang *et al.* [1] assume that this moment lies in the  $x$ - $y$  plane and so it is affected only by  $B_x$ . We therefore account for it by including a term

$$\Delta F = -g\mu_B (|\psi_\uparrow|^2 - |\psi_\downarrow|^2) B_{\parallel} \quad (2.42)$$

in our free-energy functional. Without this term, it would be possible to obtain analytic, London-limit expressions for the magnetization curves as in [24]. That this term affects the magnitudes of the superfluid densities unequally and in a non-homogeneous way is what makes undertaking numerical solutions necessary, even for highly symmetric geometries.

## 2.4 Anisotropy

The superconductor Sr<sub>2</sub>RuO<sub>4</sub> posseses a layered perovskite structure as shown in figure 2.5. The superconductivity is strongest in the metallic planes, which are weakly linked to each other in the  $z$ -direction. As such, the current response in the  $z$ -direction is suppressed relative to the  $x$ - and  $y$ -directions.

Anisotropic behavior is common to other perovskite superconductors, such

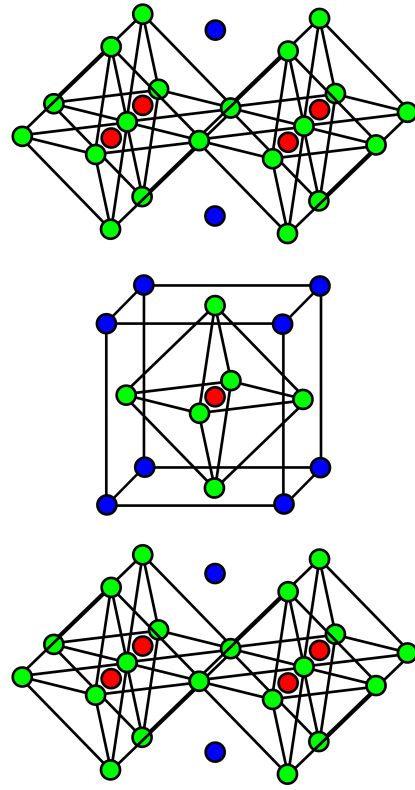


Figure 2.5: A unit cell of the layered perovskite structure of  $\text{Sr}_2\text{RuO}_4$ . Ruthenium ions are red, strontium ions are blue, and oxygen ions are green.

as the cuprates and other high-temperature superconductors. A model of 2D superconducting planes weakly linked in the  $z$ -direction was proposed by Lawrence and Doniach[25]. In the limit that  $\psi$  varies slowly in the  $z$ -direction relative to the interplanar separation, this model reduces to the anisotropic Ginzburg-Landau model. In the anisotropic Ginzburg-Landau model, the scalar mass  $m^*$  is replaced with a mass tensor  $M^*$  so that the free energy becomes[26]

$$\begin{aligned} F[\psi, \psi^*, \mathbf{A}] = & \int_{\Omega} d^3x \left\{ \frac{\hbar^2}{2} \left( \nabla + \frac{2ie}{\hbar} \mathbf{A} \right) \psi^* \cdot (M^*)^{-1} \cdot \left( \nabla - \frac{2ie}{\hbar} \mathbf{A} \right) \psi + \right. \\ & \left. + \alpha |\psi|^2 + \frac{\beta}{2} |\psi|^4 + \frac{1}{2\mu_0} |\nabla \times \mathbf{A} - \mathbf{B}_{\text{ext}}|^2 \right\}. \quad (2.43) \end{aligned}$$

We choose a coordinate system such that the crystal  $ab$  planes lie in the  $xy$ -plane and are displaced from each other in the  $z$  direction. Then, the effective mass tensor takes the form

$$M^* = \text{diag}(m_{\parallel}, m_{\parallel}, m_{\perp}). \quad (2.44)$$

We can now define penetration depths and correlation lengths for both in-plane and c-axis gradients. If we dedimensionalize the free energy by measuring

Parameter	$ab$	$c$
$B_c(0)$ (T)	0.023	
$\xi(0)$ (nm)	66	3.3
$\lambda(0)$ (nm)	152	3000
$\kappa(0)$	2.3	46

Table 2.1: Table of the measured Ginzburg-Landau parameters of  $\text{Sr}_2\text{RuO}_4$ .

lengths in units of

$$\lambda_{\parallel} = \sqrt{\frac{\beta m_{\parallel}}{4\mu_0 e^2 |\alpha|}}, \quad (2.45)$$

magnetic fields in units of  $\sqrt{2}B_{c1}$  and the order parameter in units of  $\psi_0$  we have

$$F[\psi, \psi^*, \mathbf{A}] = \int_{\Omega} d^3x \left\{ \left( \frac{1}{\kappa} \nabla - i\mathbf{A} \right) \psi^* \cdot (M_{red}^*)^{-1} \cdot \left( \frac{1}{\kappa} \nabla + i\mathbf{A} \right) \psi + \text{sgn}(\alpha) |\psi|^2 + \frac{1}{2} |\psi|^4 + |\nabla \times \mathbf{A} - \mathbf{B}_{\text{ext}}|^2 \right\} \quad (2.46)$$

where the ratio  $M_{red}^* = \text{diag}(1, 1, \gamma)$  is the reduced effective mass tensor and

$$\gamma = \frac{m_{\perp}}{m_{\parallel}} = \left( \frac{\lambda_{\perp}}{\lambda_{\parallel}} \right)^2 \quad (2.47)$$

can be calculated from the measured penetration depths  $\lambda_{\perp}$  and  $\lambda_{\parallel}$  of  $\text{Sr}_2\text{RuO}_4$  and is found to be approximately 400. Table 2.1 lists the various Ginzburg-Landau parameters of  $\text{Sr}_2\text{RuO}_4$  from [11]. Note that since  $\xi(0)_c = 3.3$  nm is still several times larger than the interplanar spacing,  $\approx 1$  nm, we are justified in using the anisotropic Ginzburg-Landau theory.

## 2.5 Full model free energy and equations of motion

The complete model free energy used in the following numerical studies can be written as

$$F[\psi, \psi^*, \mathbf{A}] = \sum_{\uparrow, \downarrow} F_0 + F_{\text{int}}. \quad (2.48)$$

The first term includes two copies of the free energy of equation (2.43), one for each field  $\psi_{\uparrow}$  and  $\psi_{\downarrow}$ . The other term includes the interactions between the two fields described in sections 2.2 and 2.3. Without de-dimensionalization, they read

$$F_{\text{int}} = \int_{\Omega} d^3x \left\{ 2b \mathbf{J}_{\uparrow} \cdot \mathbf{J}_{\downarrow} - g\mu_B (|\psi_{\uparrow}|^2 - |\psi_{\downarrow}|^2) |B_{\parallel}| \right\}. \quad (2.49)$$

Writing  $b \equiv \xi^2 \beta \tilde{b}$  and  $\mu \equiv g\mu_B \equiv \frac{|\alpha|}{\sqrt{2}B_c} \tilde{\mu}$  we can produce the dimensionless quantity

$$\tilde{F}_{\text{int}} = \int_{\Omega} d^3\tilde{x} \left\{ 2\tilde{b}\tilde{\mathbf{J}}_{\uparrow} \cdot \tilde{\mathbf{J}}_{\downarrow} - \tilde{\mu} \left( |\tilde{\psi}_{\uparrow}|^2 - |\tilde{\psi}_{\downarrow}|^2 \right) |\tilde{B}_{\parallel}| \right\} \quad (2.50)$$

which gives the free-energy terms in units of  $\lambda^2|\alpha|^2/\beta$ , as before.

Suppressing the tildes, the full, dimensionless, anisotropic free-energy reads

$$\begin{aligned} F[\psi_{\uparrow}, \psi_{\downarrow}, \mathbf{A}] = \int_{\Omega} d^3x & \left\{ \sum_{\uparrow, \downarrow} \left[ \left( \frac{\nabla}{\kappa} - i\mathbf{A} \right) \psi_i^* \cdot (M^*)^{-1} \cdot \left( \frac{\nabla}{\kappa} + i\mathbf{A} \right) \psi_i \right. \right. \\ & + \text{sgn}(\alpha)|\psi_i|^2 + \frac{1}{2}|\psi_i|^4 \Big] + |\nabla \times \mathbf{A} - \mathbf{B}_{\text{ext}}|^2 \\ & \left. \left. + 2b\mathbf{J}_{\uparrow} \cdot (M^*)^{-1} \cdot \mathbf{J}_{\downarrow} - \mu \left( |\psi_{\uparrow}|^2 - |\psi_{\downarrow}|^2 \right) B_{\parallel} \right\}. \right. \end{aligned} \quad (2.51)$$

Minimizing this functional with respect to  $\psi_{\uparrow}^*$ ,  $\psi_{\downarrow}^*$ , and  $\mathbf{A}$  gives us

$$\begin{aligned} \frac{\delta F}{\delta \psi_{\uparrow}^*} = -\frac{\nabla}{\kappa} \cdot (M^*)^{-1} \cdot & \left[ \left( \frac{\nabla}{\kappa} - i\mathbf{A} \right) \psi_{\uparrow} + ib\psi_{\uparrow}\mathbf{J}_{\downarrow} \right] \\ & + (\text{sgn}(\alpha) + |\psi_{\uparrow}|^2 + |\mathbf{A}|^2 - 2b\mathbf{J}_{\downarrow} \cdot (M^*)^{-1} \cdot \mathbf{A})\psi_{\uparrow} \\ & + i\frac{\nabla}{\kappa} \psi_{\uparrow} \cdot (M^*)^{-1} \cdot (\mathbf{A} - b\mathbf{J}_{\downarrow}) - \mu\psi_{\uparrow}B_{\parallel}, \end{aligned} \quad (2.52)$$

$$\begin{aligned} \frac{\delta F}{\delta \psi_{\downarrow}^*} = -\frac{\nabla}{\kappa} \cdot (M^*)^{-1} \cdot & \left[ \left( \frac{\nabla}{\kappa} - i\mathbf{A} \right) \psi_{\downarrow} + ib\psi_{\downarrow}\mathbf{J}_{\uparrow} \right] \\ & + (\text{sgn}(\alpha) + |\psi_{\downarrow}|^2 + |\mathbf{A}|^2 - 2b\mathbf{J}_{\uparrow} \cdot (M^*)^{-1} \cdot \mathbf{A})\psi_{\downarrow} \\ & + i\frac{\nabla}{\kappa} \psi_{\downarrow} \cdot (M^*)^{-1} \cdot (\mathbf{A} - b\mathbf{J}_{\uparrow}) + \mu\psi_{\downarrow}B_{\parallel}, \end{aligned} \quad (2.53)$$

and

$$\frac{\delta F}{\delta \mathbf{A}} = \nabla \times \nabla \times (\mathbf{A} - \mathbf{B}_{\text{ext}}) - (\mathbf{J}_{\uparrow} + \mathbf{J}_{\downarrow}) - b(|\psi_{\uparrow}|^2\mathbf{J}_{\downarrow} + |\psi_{\downarrow}|^2\mathbf{J}_{\uparrow}). \quad (2.54)$$

Here, the dimensionless current is

$$\mathbf{J}_i = \frac{1}{2i} \left[ \psi_i^* \left( \frac{\nabla}{\kappa} - i\mathbf{A} \right) \psi_i - \psi_i \left( \frac{\nabla}{\kappa} + i\mathbf{A} \right) \psi_i^* \right] \quad (2.55)$$

which give the current in units of  $|\alpha|/\xi\beta$ .

The associated boundary conditions are

$$\hat{\mathbf{n}} \cdot (M^*)^{-1} \cdot \left[ \left( \frac{\nabla}{\kappa} - i\mathbf{A} \right) \psi_{\uparrow} + ib\psi_{\uparrow}\mathbf{J}_{\downarrow} \right] = 0, \quad (2.56)$$

$$\hat{\mathbf{n}} \cdot (M^*)^{-1} \cdot \left[ \left( \frac{\nabla}{\kappa} - i\mathbf{A} \right) \psi_{\downarrow} + ib\psi_{\downarrow}\mathbf{J}_{\uparrow} \right] = 0, \quad (2.57)$$

and

$$\nabla \times (\nabla \times \mathbf{A} - \mathbf{B}_{\text{ext}}) = 0, \quad (2.58)$$

to be satisfied at the boundary of the superconductor. One will notice that these equations reduce to the usual Ginzburg-Landau equations and boundary conditions, if  $b$  and  $\mu$  are set equal to zero.

# 3 Numerical Method

## 3.1 Equations and boundary conditions

My goal was to calculate equilibrium magnetization curves that can be directly compared with those in [1] (see figures 1.1 and 1.2). Because of the asymmetric and three-dimensional character of the experimental samples, these curves have to be found numerically. The finite-element method is a natural tool for handling the highly asymmetric geometries involved. Of the many published numerical solutions to the Ginzburg-Landau equations (a small sampling includes [27, 28, 29]), the vast majority are of two-dimensional regions. Most do not adequately treat the energy of magnetic field surrounding the superconducting region nor do they seek to accurately calculate magnetization curves. Because of the lack of collective experience in this endeavor, I had to be led by bitter experience to a consistent and robust method of finding accurate solutions.

I seek the local minima (potentially metastable states) by choosing initial data and sliding down the free-energy hill via

$$\frac{\partial \mathbf{A}}{\partial t} = -\frac{\delta F}{\delta \mathbf{A}}; \quad \frac{\partial \psi_i}{\partial t} = -\frac{\delta F}{\delta \psi_i^*}. \quad (3.1)$$

Note the interchange of  $\psi$  and  $\psi^*$  between the two sides of the last equation. This is because we have used the metric defined by

$$||\delta\psi||^2 = \int_{\Omega} d^3x |\delta\psi|^2 \quad (3.2)$$

to convert the functional derivative (a covector) into a gradient (a vector) in function space. The necessary functional derivatives  $\delta F/\delta \mathbf{A}$ , and  $\delta F/\delta \psi_i^*$  are given in equations (2.52), (2.53), and (2.54).

The computational geometry is determined by attempting to define a superconducting region as close to the real sample geometry as possible. This sample is then embedded in a large cylindrical volume as depicted in figure 3.3. For the boundary conditions of the vector potential, we can establish the externally imposed magnetic field  $\mathbf{B} = (B_x, B_y, B_z)$  by imposing the inhomogeneous

Dirichlet boundary conditions

$$\begin{aligned} A_x &= \frac{1}{2}(B_y z - B_z y), \\ A_y &= \frac{1}{2}(B_z x - B_x z), \\ A_z &= \frac{1}{2}(B_x y - B_y x). \end{aligned} \quad (3.3)$$

on the surface  $\partial\Omega$  of the cylinder.

The first calculations I performed and reported in my preliminary examination were of rings with weak link Josephson junctions given in Appendix B. Initially my advisor and I thought it would be simplest not to impose the natural boundary conditions for the order-parameters, given in equations (2.56) and (2.57), at the boundary of the superconductor, but to simply set  $\text{sgn}(\alpha)=-1$  in the superconducting volume, along with  $\text{sgn}(\alpha)=+1$  in the surrounding volume. This is equivalent to modelling a superconductor embedded in a normal metal. The subsequent proximity effect prohibits one from making a correspondence between the volume with  $\text{sgn}(\alpha)=-1$  and the physical superconductor. This was very striking in the studies of rings with weak links because the volume in which  $\text{sgn}(\alpha)=-1$  was not multiply connected and yet the system showed periodic fluctuations in free energy and magnetic moment. This led us to impose the “natural” boundary conditions that arise from the variational problem of free energy minimization. In other words, we require the vanishing of the integrated out variation terms on the surface of the superconductor. This leads to

$$\begin{aligned} \mathbf{n} \cdot (M_{\text{red}}^*)^{-1} \cdot \left( \frac{\nabla}{\kappa} - i\mathbf{A} - \frac{\tilde{\beta}}{\kappa} \mathbf{J}_\downarrow \right) \psi_\uparrow &= 0 \\ \mathbf{n} \cdot (M_{\text{red}}^*)^{-1} \cdot \left( \frac{\nabla}{\kappa} - i\mathbf{A} - \frac{\tilde{\beta}}{\kappa} \mathbf{J}_\uparrow \right) \psi_\downarrow &= 0 \end{aligned} \quad (3.4)$$

on the surface of the superconducting ring.

I find the fields that minimize the free energy by first choosing initial conditions for the magnetic vector potential and for the order-parameter fields, and then allow them to relax to a (local) minimum in free-energy via equations (3.1). I can then integrate  $(\mathbf{r} \times \mathbf{J})_z$  over the volume to find the magnetic moment in the  $z$ -direction. We initially thought that we could simply calculate the results of starting the system in the state  $\psi_\uparrow = \psi_\downarrow = 1$ ,  $\mathbf{B}_{\text{ext}} = 0$  at  $t = 0$  and linearly increase the magnetic field. Unfortunately this doesn’t capture the proper physics due to an effect I refer to as numerical hysteresis. In nature, the transition from one fluxoid state to another is expedited by thermally activated vortices. In my equations I do not have any terms modelling thermal fluctuations. This leads to the transitions between fluxoid states being delayed, making it impossible to capture the correct periodicity. Simply adding randomly varying terms to the pseudopotential has little effect as these are not the right type of fluctuations.

What one would like to simulate are vortex fluctuations, for which it would be very difficult to write analytic expression.

I then tried a method similar to what was done in the experiment of [1] called “field-cooling”. I set  $\text{sgn}(\alpha)=+1$  at  $t = 0$  along with  $\mathbf{B}_{\text{ext}}$  to the desired value. Then,  $\text{sgn}(\alpha)$  was continuously lowered until it equalled  $-1$ . I hoped that the order-parameter would instantiate itself in with the correct winding number. Unfortunately, this method was unreliable as can be seen in figure 3.1. The system jumps between fluxoid states in an almost random fashion. It is impossible to draw from this the correct periodicity.

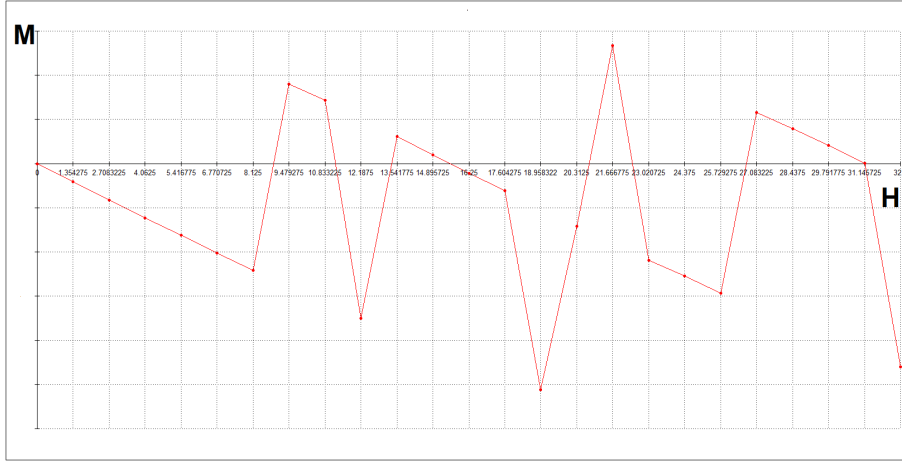


Figure 3.1: Illustrating the unreliability of the field-cooled results.

After these failures, I developed a strategy based on calculating the magnetization curves via the formula  $-\partial F/\partial B_{\text{ext}}$ . I begin by imposing the initial conditions

$$\psi_{\uparrow} = \exp[in_{\uparrow}\phi]; \quad \psi_{\downarrow} = \exp[in_{\downarrow}\phi] \quad (3.5)$$

that correspond to a selected flux state. (Here,  $\phi$  is the azimuthal angle around the ring. For instance,  $(n_{\uparrow}, n_{\downarrow}) = (0, 0)$  corresponds to the zero flux state while  $(1, 0)$  and  $(0, 1)$  correspond to half-flux states.)

After selecting the desired winding numbers and setting the externally imposed magnetic field, I allow the system to relax to a local minimum of the free energy. This free energy is then calculated by evaluating the integral in (2.51). In this way we are able to construct diagrams of free energy versus applied magnetic field in the  $z$ -direction for different flux states and for different values of in-plane magnetic field. These diagrams reveal which flux state is energetically favorable at each value of applied  $z$ -axis field. Using these, I numerically compute the derivatives of the free energy with respect to the applied  $z$ -axis field, and thus construct the magnetization curves.

I will focus on the results for the single annular sample shown in figure 3.3. The ring’s inner radius is  $2 \lambda_{||}$  while the outer radius averages  $5.29 \lambda_{||}$  where  $\lambda_{||}(T = 0)$  is given as 152 nm for  $\text{Sr}_2\text{RuO}_4$  in [11]. The height of the sample

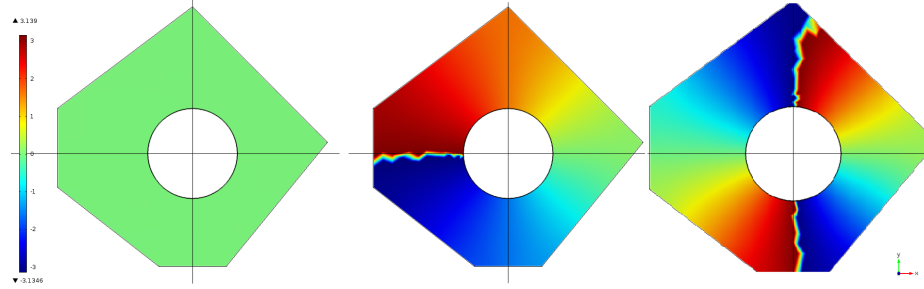


Figure 3.2: Temperature plots of the phase in states with winding number  $n=0$ ,  $n=1$ , and  $n=2$ .

is  $1.7 \lambda_{||}$ . This geometry is designed to approximate the experimental sample shown in Figure [1.1]. The ring is centered in a cylindrical volume  $\Omega$  of height  $20 \lambda_{||}$  and radius  $20 \lambda_{||}$ . The dimensions of the cylinder were chosen to balance the competing effects of increased computation time for larger cylinders against spuriously high magnetic field energies caused by confining the field in too small a volume.

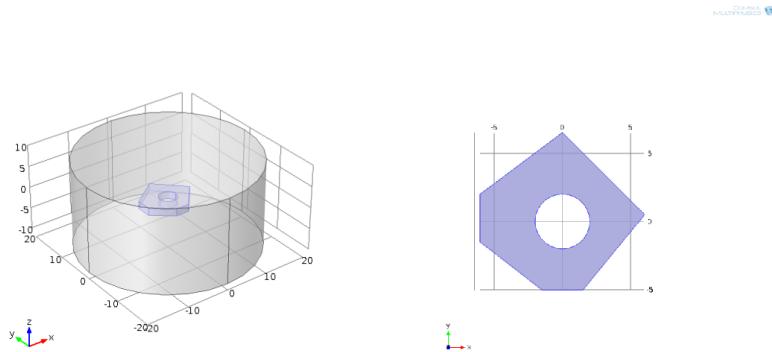


Figure 3.3: On the left is shown a representation of the simulated geometry. On the right is a top-down view of the simulated ring. The axes in both figures are labelled in units of  $\lambda_{||}$ .

# 4 Results

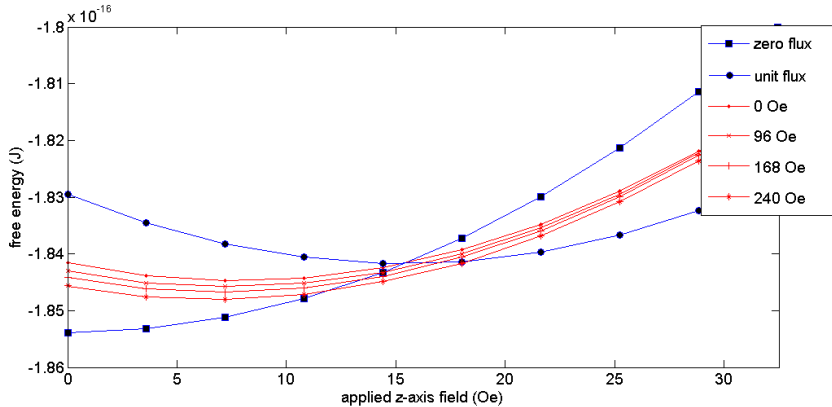


Figure 4.1: This figure shows an example of calculated relative free energies of the integer and half-flux states near the first transition. Each red line represents the free energy of the half-flux state at different values of applied in-plane magnetic field. Higher magnetic fields are seen to result in relatively lower free energies of the half-flux state.

Figure 4.1 illustrates the free energy of the system versus applied z-axis field (from 0 to 32.5 Gauss), and for a few values of applied in-plane magnetic field. The blue line depicts the  $(0,0)$  and  $(1,1)$  integer-flux states while the red line depicts the  $(1,0)$  half-flux state.<sup>1</sup> One can see from the diagram that the half-flux state has a reduced free energy versus the integer-flux states for higher values of in-plane field.

Applying a parabolic fit to the free energy curves, one can take the derivative with respect to the applied magnetic field to obtain magnetization curves. Figure 4.2 displays magnetization curves versus z-axis field for various values of in-plane field, as in Figure 2. The magnetization curves are seen to be qualitatively similar to the experimental curves of figure 1.2. By adjusting  $\tilde{b}$  and  $\tilde{\mu}$  one may obtain the desired minimum in-plane stabilization field and stability region growth rate.

The dimensionless current-current coupling parameter  $\tilde{b}$  can be related to

---

<sup>1</sup>Applying an in-plane field produces a spin polarization for both integer and half integer flux states. We have plotted the data so as to show only the *relative* free energy of the integer and half-integer states. We did this by shifting all curves by an in-plane-field dependent constant so that the integer-flux state's data overlap one another.

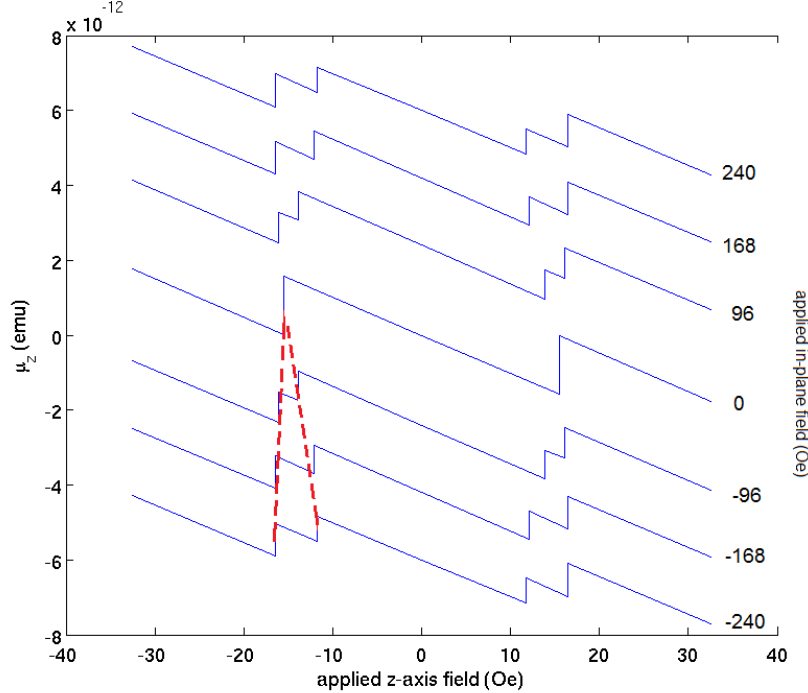


Figure 4.2: Computed magnetization curves obtained using  $\rho_{sp}/\rho_s = 0.25$  and a magnetic dipole moment of  $0.55\mu_B$ .

the ratio of the spin and charge fluid densities via

$$\frac{\rho_{sp}}{\rho_s} = \frac{1 - \tilde{b}}{1 + \tilde{b}}. \quad (4.1)$$

Typical values of  $\tilde{b}$  which matched the experimental data were 0.4-0.6 corresponding to  $\rho_{sp}/\rho_s$  between 0.25 and 0.43.

If  $\tilde{\mu}$  is interpreted as the magnetic dipole moment per particle of the spin condensate, it gives a magnetic dipole moment in units of  $\sqrt{2}e^2B_c\lambda^2m_e^{-1}$ . Using  $B_c = 230$  Oe and  $\lambda = 152$  nm, the value of this unit is approximately  $2.12 \times 10^{-23} J/T \approx 2.2\mu_B$ . Typical values of the magnetic dipole moment that fit the data were found to be around  $0.6\mu_B$ .

The magnitude of the in-plane spin magnetic moment for the case of 240 Oe in-plane field is plotted in Figure 4.3. When the applied z-axis field is near zero, the system is in the  $(n_\uparrow, n_\downarrow) = (0, 0)$  state. The presence of the in-plane magnetic field induces an in-plane magnetic moment even in the absence of kinematic spin polarization. Thus, there is a non-zero moment even in the integer flux states. The presence of kinematic spin polarization accounts for the sudden increase in moment at the transition to the half-flux state near 12 Oe. This additional moment vanishes when the system transitions to the unit fluxoid state at 16 Oe.

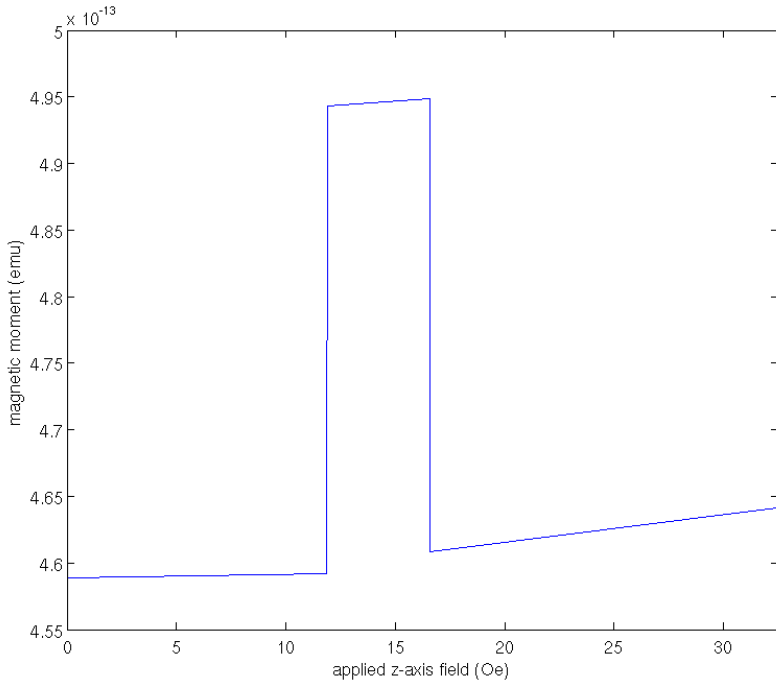


Figure 4.3: The calculated in-plane spin magnetic moment for 200 Oe of applied in-plane field.

## 4.1 Abrikosov Vortices

As discussed in [1], the half-step magnetization jumps in Figure 1.2 may be explained by unique Abrikosov vortex configurations in a simple s-wave order parameter. In the applied field configurations where a half-flux quantum is detected, a vortex could pierce the sample through the sidewall precisely halfway between the top and bottom of the ring. The vortex could then bend and exit the top or bottom without piercing the other side. In this way, half of the ring could contain a flux winding and could produce a half-step of magnetization.

I examined this possibility by first examining at what magnitude of applied in-plane field an Abrikosov vortex piercing the sample in the x-direction becomes energetically favorable. Using the numerical technique described in the previous section with the usual s-wave Ginzburg-Landau model, I gave the system the initial condition of having a flux winding about the x-direction (i.e.,  $\psi = \exp[i \arctan(z/y)]$ ). With COMSOL we are able to view the solution of order parameter, as in Figure 4.4. The free energy of this configuration was then compared to one with no flux winding in the sample. The results for the sample of interest is shown in Figure 4.5. As can be seen in the figure, the vortex becomes stable near 350 Oe of applied in-plane field, which is greater than the region of in-plane field where the half-steps in flux quantization are first seen. This is consistent with the experiment discussed in [1].

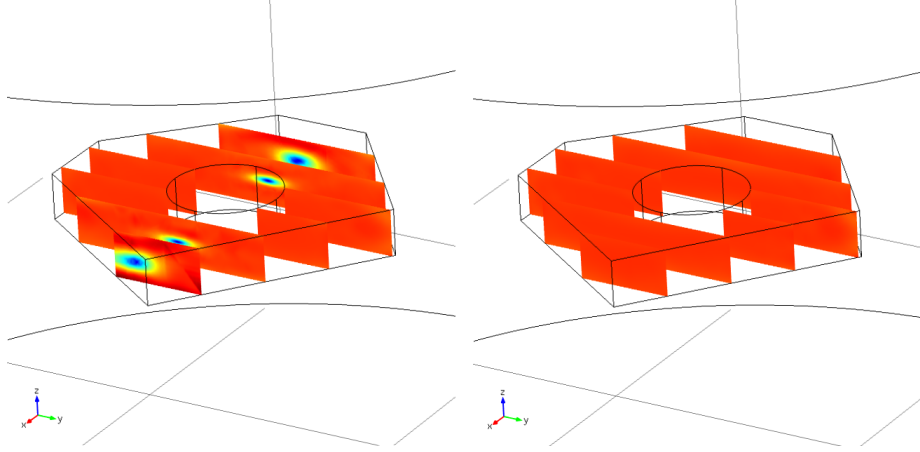


Figure 4.4: Slices through the sample plotting the magnitude of the order parameter. Darker areas indicate lower values of the order parameter while brighter regions indicate higher values. On the left is the sample penetrated by a vortex oriented in the x-direction. On the right is the sample without any Abrikosov vortices.

An analytic result for  $H_{c1}||ab$  in similarly sized samples of anisotropic superconductors is given in [30] as  $H_{c1}||ab = (2\gamma\Phi_0/\pi L_y^2)\ln(L_y/\pi\xi_{ab})$  where  $\gamma$  is the anisotropy parameter  $\lambda_\perp/\lambda_\parallel$ ,  $L_y$  is the sample size in the ab-plane, and  $\xi_{ab}$  is the GL coherence length in the ab-plane. Using the values for our simulated sample of  $\gamma = 20$ ,  $L_y = 1600$  nm, and  $\xi_{ab} = 66$  nm, this formula gives 210 Oe, which is in reasonable agreement with the numerical result. A similar result was obtained for the sample considered in [1] where the estimated value of  $H_{c1}$  was 150 Oe, while the measured value was somewhat higher at 250 Oe. These results indicate that we should not expect to see Abrikosov vortex penetration until the in-plane field is of much greater magnitude than where half-flux states are detected.

I attempted to examine the stability of the bent vortex configuration by giving the system the same initial condition  $\psi = \exp[i \arctan(z/y)]$  as shown in Figure 4.4. If the bent vortex configurations were energetically favorable, one expects the system to evolve from the initial condition to one with a bent vortex. Despite numerous trials with magnetic field configurations in which we saw a half-quantum vortex in the two-fluid model, I was unable to achieve a stable bent-vortex configuration. The vortex either left the sample completely or remained penetrating the entire sample. I recognize that this is not definitive, but it does show the difficulty in stabilizing such a configuration.

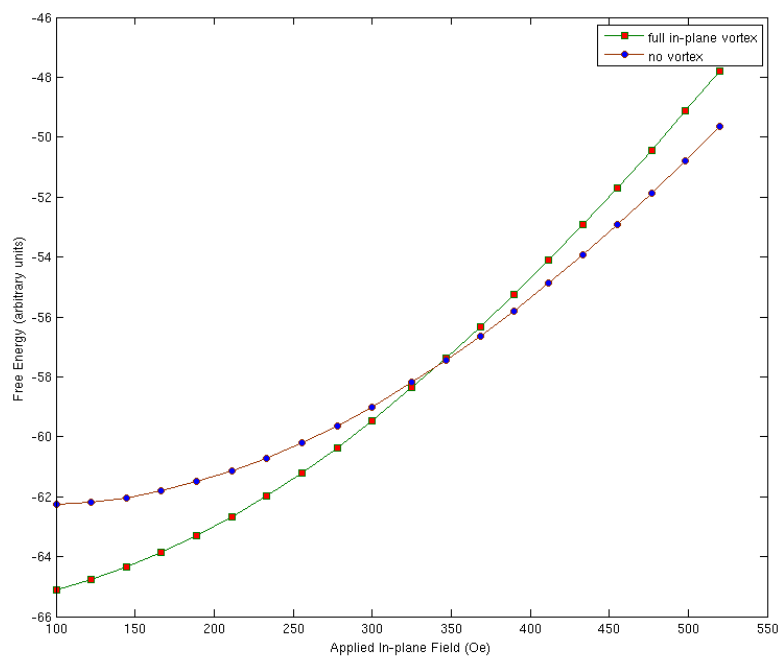


Figure 4.5: The free energies of a vortex oriented in the x-direction versus no vortex.

# 5 Vortex Energetics and Magnetoresistance Oscillations

The preceding results were qualitative in nature. However, an observant reader will notice a large difference in the magnitudes of the magnetic moments plotted in figures 1.2 and 4.2 despite the numerical calculations being performed using a sample size and shape similar to the experimental setup. At a given field, the numerical calculations yield a magnetic moment  $\approx 40$  times larger than the experimental sample. What is not evident from the preceding discussion is that this effect seems to be limited to samples with a diameter  $\sim 1\mu\text{m}$  or smaller.

As a means of obtaining an order-of-magnitude approximation, consider a model of the superconducting rings as an infinite solenoid maintaining a perfect Meissner state. The magnetic moment, in this case, is  $\mu = B_{\text{ext}}V/\mu_0$ , where  $V$  is the sample volume. For a sample of  $1\mu\text{m} \times 1\mu\text{m} \times 0.5\mu\text{m}$ , similar to the samples in [1], this formula gives  $\approx 4 \times 10^{-11}\text{e.m.u.}$  at a field of 10 Oe, significantly larger than the measured values of  $\approx 1 \times 10^{-13}\text{ e.m.u..}$  Compare this case to a larger sample of  $5\mu\text{m} \times 4\mu\text{m} \times 2\mu\text{m}$ , such as the one featured in [2], whose magnetization curves are reproduced here in figure 5.1. The crude solenoid model gives an estimate of  $3 \times 10^{-12}\text{ e.m.u.}$ , in good agreement with the data of figure 5.1.

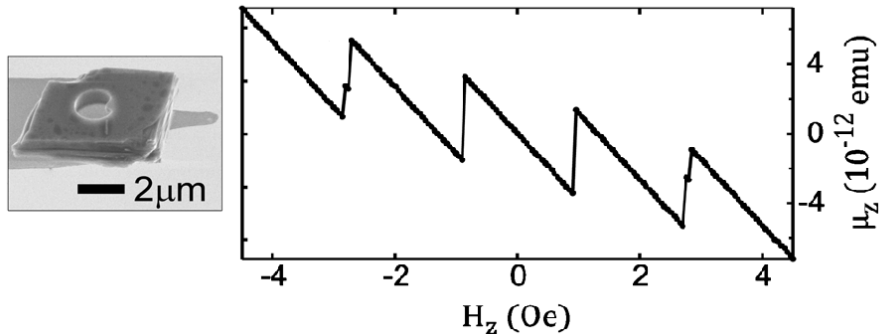


Figure 5.1: Magnetization curves for a sample with a diameter of  $\approx 5\mu\text{m}$ . Adapted from [2].

$T_c$  is strongly suppressed by non-magnetic impurities in materials with exotic pairing mechanisms such as the cuprates and  $\text{Sr}_2\text{RuO}_4$ [11, 31, 32], presumably due to scattering that averages  $\mathbf{k}$ -states near the Fermi surface with opposite phase. It is natural to expect that the order parameter in such materials is greatly suppressed near the surface leaving a layer of depth  $\sim \xi$  with negligible

magnetization and greatly increasing the effective penetration depth. Given the correlation length in  $\text{Sr}_2\text{RuO}_4$  of 50-100 nm, the effect of this mechanism on the magnetization should be negligible in macroscopic sample sizes. However, for the mesoscopic samples used in [1], one would expect this effect to be significantly enhanced as the suppressed region would make up a much larger proportion of the sample. This idea is shown scematically in figure 5.2.

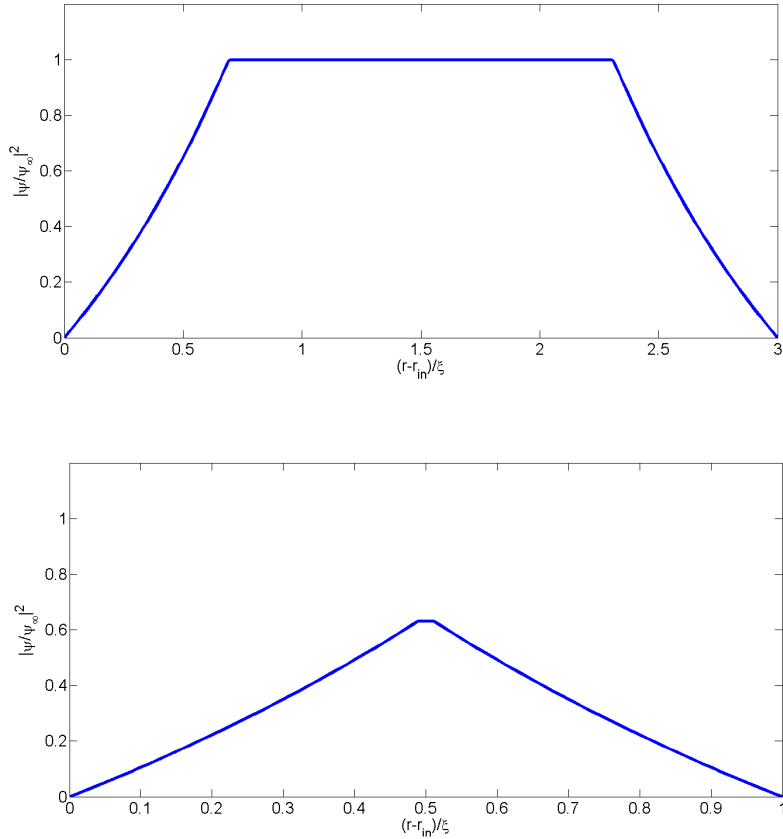


Figure 5.2: For a sample of smaller size, the suppression of the order-parameter near the edges has a more pronounced effect on the overall average magnitude and penetration depth.

In the rest of this chapter we try to put this idea on a more quantitative footing. There have recently been attempts by a group at Penn State University to measure the presence of half-quantum vortices in  $\text{Sr}_2\text{RuO}_4$  via signatures in magnetoresistance oscillations[4]. Such measurements are very sensitive to the potential barrier for vortex entry making calculations of this type important.

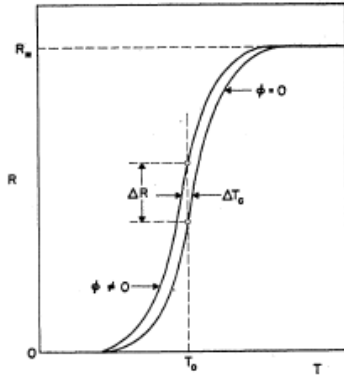


Figure 5.3: The resultant change in resistance due to a shift in  $T_c$ .

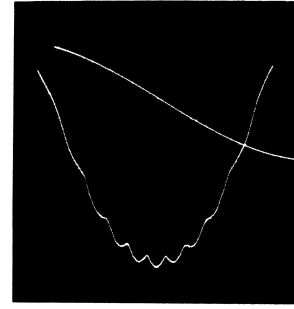


Figure 5.4: Data from [3]. The upper trace plots the applied magnetic field.

## 5.1 Theory of Magnetoresistance Oscillations in Thin Rings

### 5.1.1 The Little-Parks Effect

Magnetoresistance oscillations indicative of flux quantization were first observed by W.A. Little and R.D. Parks in a thin cylinder of tin in 1962[3]. The magnetoresistance oscillations in tin and other s-wave superconductors known before the discovery of the cuprates could be explained as oscillations in  $T_c$  as a function of the applied magnetic field. The change in resistance is then given by  $\Delta R = (dR/dT)\Delta T_c$  as shown in figure 5.3. This phenomenon is known as the Little-Parks effect.

For the case of a thin-walled, infinitely long superconducting cylinder of width  $w$ , Groff and Parks[33] give the variation of  $T_c$  as

$$\frac{\Delta T_c}{T_c} = \frac{\xi(0)^2}{r_m^2} \left[ \left( n - \frac{\Phi}{\Phi_0} \right)^2 (1 + a^2) + \frac{4}{3} n'^2 a^2 \right] \quad (5.1)$$

where  $\xi(0)$  is the zero-temperature coherence length,  $r_m = (r_{\text{outer}} - r_{\text{inner}})/2$ ,  $\Phi = \pi r_m^2 H$ ,  $a = w/2r_m$ ,  $H$  the applied field, and  $n' = n/(1 + a^2)$ . Here,  $n$  is the winding number of the order-parameter about the cylinder, and is chosen to maximize  $T_c(H)$  as the field increases.

While the Little-Parks effect adequately describes the magnetoresistance oscillations in the s-wave superconductors known in the 1960's, it fails to explain the oscillations observed in superconductors with exotic pairing mechanisms and smaller correlations lengths such as  $\text{La}_{2-x}\text{Sr}_x\text{CuO}_4$ [34, 15] and  $\text{Sr}_2\text{RuO}_4$ [4]. Figure 5.4 shows the experimental setup and data reported in [4]. The resistance was measured in a micron-sized annulus of  $\text{Sr}_2\text{RuO}_4$  etched by a focused ion beam. The oscillations predicted by the Little-Parks effect and equation

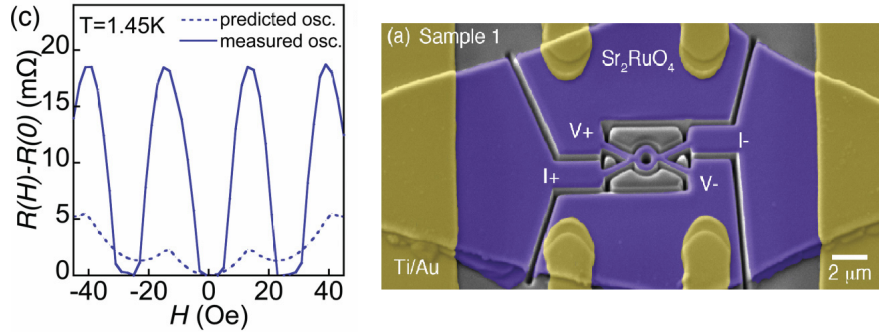


Figure 5.5: The experimental setup and data reported in [4]. The dotted line shows the resistance oscillations predicted by 5.1. Adapted from [4].

(5.1), shown by the dotted line, are an order of magnitude too small to explain the measured resistance. This is due to the dependence of equation 5.1 on  $\xi^2$ . Small correlation lengths pose a problem to explaining the observed resistance via the Little-Parks effect but also point the way to a solution. Since materials for which these phenomena occur are in the Type II regime they support vortices and vortices crossing the walls of the superconducting ring will cause a phase difference and thus, a voltage, across the sample.

### 5.1.2 Vortex-Induced Magnetoresistance Oscillations

Sochnikov et. al. [15] have proposed a theory of magnetoresistance oscillations driven by the passage of vortices into and out of multiply connected superconductors. Their theory hinges on Ambegaokar and Halperin's result[35], which shows that the resistance induced by thermal fluctuations in heavily damped Josephson junctions in the limit of small currents is given by

$$\frac{R}{R_n} = [I_0(\gamma_0/2)] \quad (5.2)$$

where  $\gamma_0 \equiv \hbar I_1(T)/eT$  and  $I_0$  is the zeroth-order modified Bessel function. Here,  $I_1(T)$  is the temperature dependent maximum Josephson current. This result was used later by Tinkham to explain the resistive transition of the cuprates[36]. Tinkham interpreted  $\gamma_0$  as the activation energy for vortex lattice creep in high-temperature superconductors. In Tinkham's own words, “not rigorously applicable to this case, their results at least provide a plausible simiquantitative model for the dependence of  $R/R_n$  on  $\gamma_0$ .”

In the theory of Sochnikov et. al. the important processes are vortices entering and exiting the multiply connected superconductor. They therefore take  $\gamma_0$  to be the thermal average of the potential barriers faced by the entry and exit of all possible vortex states. In practice, it is necessary only to consider the

entry and exit of a vortex(+) and anti-vortex(-) with winding numbers +1 and -1, respectively. This expression can be written concretely as

$$\Delta E = \sum_{\substack{i \in \text{in, out} \\ j \in +,-}} \Delta E_i^j e^{-\Delta E_i^j / k_B T} / \sum_{\substack{i \in \text{in, out} \\ j \in +,-}} e^{-\Delta E_i^j / k_B T}. \quad (5.3)$$

The task remains to find the potential barriers  $\Delta E_i^j$ . It is fruitful to take advantage of the useful London theory solutions of a thin, superconducting ring given by Kogan, Clem, and Mints[17]. Consider a superconducting ring that has a thickness  $d$  comparable to the superconducting coherence length and whose largest dimension is much smaller than the Pearl length  $\Lambda \equiv 2\lambda^2/d$ , where  $\lambda$  is the superconducting penetration depth, an analytic expression for the free energy of the ring can be calculated. Kogan, Clem, and Mints give the free energy of a small, thin superconducting ring of inner radius  $a$  and outer radius  $b$  as

$$\mathcal{F}_\pm(N, v, H) = \epsilon_v(v) + \epsilon_0 \left[ \left( N \pm \frac{\ln(b/v)}{\ln(b/a)} \right)^2 - 2h \left( N \pm \frac{b^2 - v^2}{b^2 - a^2} \right) + h^2 \chi \right]. \quad (5.4)$$

The free energy is given as a function of the winding number of the order parameter around the central hole  $N$ , the radius of an Abrikosov vortex  $v$ , and the applied magnetic field  $H$ . The  $\pm$  indicates which direction the order parameter winds around the vortex. If there is a “+” Abrikosov vortex penetrating the ring at a radius  $a < v < b$ , the winding number of the order parameter at  $r = a$  will be  $N$  while at  $r = b$  it is  $N + 1$ . Similarly, the winding number will be  $N - 1$  for a “-” vortex. The quantity  $\epsilon_v(v)$  is the self-energy of the Abrikosov vortex and is given by

$$\epsilon_v \approx \frac{\phi_0^2}{8\pi^2\Lambda} \ln \left[ \frac{2v \ln(b/a)}{\pi\xi} \sin \frac{\pi \ln(v/a)}{\ln(b/a)} \right]. \quad (5.5)$$

The quantity  $\epsilon_0 \equiv \phi_0^2 \ln(b/a)/8\pi^2\Lambda$  and  $h = H/H_0$  where  $H_0 = 2\phi_0 \ln(b/a)/\pi(b^2 - a^2)$  is the period of ring. The quantity  $\chi$  is a geometric factor of order unity given by

$$\chi = \frac{b^2/a^2 + 1}{b^2/a^2 - 1} \ln \frac{b}{a}. \quad (5.6)$$

Equations (5.4) and (5.5) involve the temperature-dependent penetration depth,  $\lambda(T)$ , and correlation length,  $\xi(T)$ . For these I used the functional forms

$$\lambda(T) = \frac{\lambda_0}{\sqrt{1 - (T/T_c)^2}} \quad (5.7)$$

and

$$\xi(T) = \frac{\xi_0}{\sqrt{1 - T/T_c}} \quad (5.8)$$

in accord with the standard formulae found in [18, Chapter 4].

The potential barriers to the entry and exit of vortices and anti-vortices as a function of vortex position can be calculated by subtracting the appropriate forms of equation (5.4). For example, the potential barrier for the entry of a vortex into a thin ring with a winding number  $N$  is

$$V_{\text{in}}^+(N, v) \equiv \mathcal{F}_+(N, v) - \mathcal{F}_0(N) \quad (5.9)$$

where  $\mathcal{F}_0(N)$  is found by setting  $v = b$  in (5.4) and the potential barrier for the exit of a vortex from a ring with winding number  $N$  is

$$V_{\text{out}}^-(N, v) \equiv \mathcal{F}_-(N + 1, v) - \mathcal{F}_0(N). \quad (5.10)$$

The maximums of  $V_{\text{out}}^+$ ,  $V_{\text{in}}^+$ ,  $V_{\text{out}}^-$ , and  $V_{\text{in}}^-$  are then used as the  $\Delta E_i^j$  in (5.3) which, in turn, can be used to calculate the resistance via (5.2).

## 5.2 Oscillations in Superconducting Rings of Sr<sub>2</sub>RuO<sub>4</sub>

Cai et. al. have published data showing unconventional magnetoresistance oscillations in mesoscopic rings of Sr<sub>2</sub>RuO<sub>4</sub>[4]. I will here analyze the energetics of two of the samples presented there. The ring-shaped samples were of roughly uniform height, but the inner and outer edges were sloped so as to give the rings a broader width at the bottom than at the top as shown in the CAD illustration of figure 5.7. The sample dimensions are shown in table 5.1.

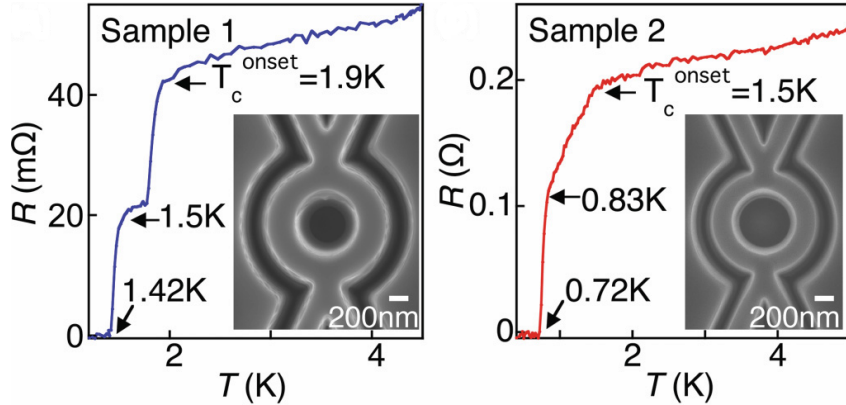


Figure 5.6: SEM images and critical temperature measurements for the two sample rings analyzed in section 5.2.

As discussed above, the size of the oscillations precludes their explanation via the Little-Parks effect. However, there is another troubling barrier to their explanation via vortex-induced phase noise. The efficacy of vortex-induced resistance depends heavily on the ratio  $\Delta E/k_B T$ , the potential energy barrier

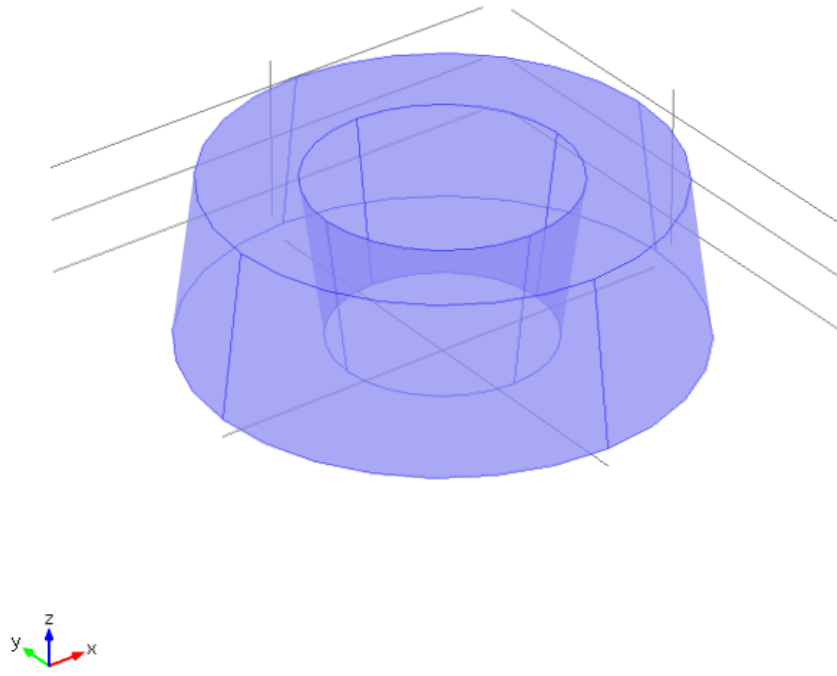


Figure 5.7: CAD illustration of the samples used in [4].

experienced by the vortex to the thermal energy. The energy barrier for a vortex crossing the ring should be on the order of  $(B_c^2/2\mu_0) * \xi_{ab}^2 d$  where  $\xi_{ab}$  is the penetration depth in the  $ab$ -plane and  $d$  is the ring height. Using  $B_c \approx 200$  Oe,  $\xi_{ab} \approx 100$  nm, and  $d \approx 400$  nm, I find the energy scale to be  $\sim 10^{-18}$  Joules. However, at temperatures on the order of 1 K,  $k_B T \approx 10^{-23}$  J. The thermal fluctuations appear to be five orders-of-magnitude too small to explain the passage of vortices numerous enough to cause a measurable resistance. For further investigation, I performed fits to the data of two samples published in [4].

If I assume a uniform width to the rings, which one would expect to be

	$r_m$	$h$	$w_{top}$	$w_{bottom}$	$w_m$	$r_m^{fit}$	$h^{fit}$	$w_m^{fit}$
Sample 1	480	450	250	390	320	500	450	250
Sample 2	440	400	160	230	195	450	410	200

Table 5.1: This table lists the mean width,  $r_m$ , height,  $h$ , width at the top,  $w_{top}$ , width at the bottom,  $w_{bottom}$ , median width  $w_m$ , and their fitted values, given in nm, of the two samples analyzed in this thesis. The measured sample dimensions are accurate to within  $\pm 10$  nm.

between the minimum and maximum values listed in table 5.1, I can use the method of calculation outlined in the previous section, attempting to fit the resistance data with the theory of resistance oscillations presented by Sochnikov et. al. in [15]. The fits were done using a MATLAB fitting tool utilizing a non-linear least squares technique. Using the measured applied magnetic field, temperature, the sample's critical temperature, and normal resistance, I fitted for the sample's inner and outer radius, height, zero-temperature penetration depth, and zero-temperature correlation length.

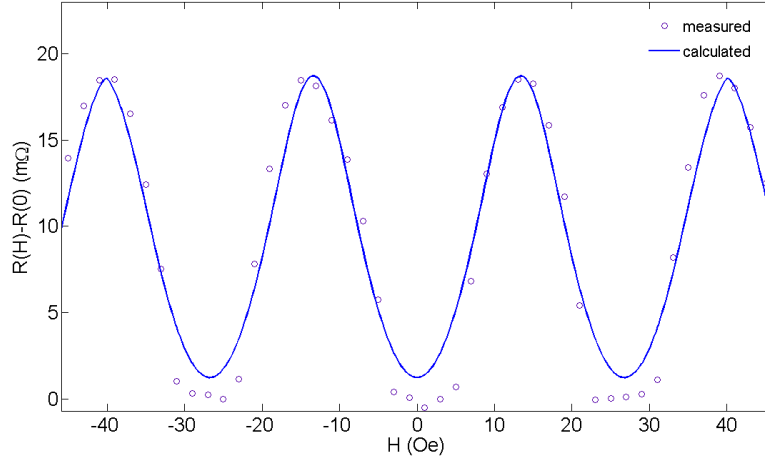


Figure 5.8: Fit of the magnetoresistance oscillations of Sample 1.

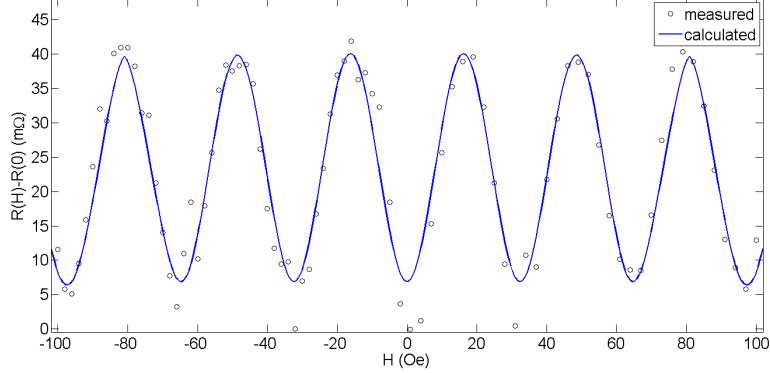


Figure 5.9: Fit of the magnetoresistance oscillations of Sample 2.

The fits are shown in figures 5.8 and 5.9. At temperatures so near  $T_c$ , the energetics were insensitive to the values of  $\xi_0$  near the quoted value of 66 nm[11, Section III.C]. The fitted values of the median radius,  $r_m^{\text{fit}}$ , height,  $h^{\text{fit}}$ , and width,  $w_m^{\text{fit}}$  are shown in table 5.1. All of the fitted values of the geometry are reasonable. This model also does a good job of capturing the correct periodicity. However, the fitted value of  $\lambda_0$  was  $\approx 11 \mu\text{m}$  for Sample 1 and  $\approx 15 \mu\text{m}$  for

Sample 2, both in gross excess of 152 nm given by [11] and justifying the use of analytic solutions applicable in the Pearl limit (dimension  $\ll (\lambda^2/2d)$ ). Given equation (2.15), this is a sign that the superconducting order parameter is being suppressed, increasing the effective penetration depth of the sample.

Victor Vakaryuk and I also examined the idea that the ease of vortex transitions into and out of the ring was facilitated by a defect near the edge of the sample. At such a defect, the order-parameter would be suppressed, making it energetically favorable for a vortex to pass into this region. And, due to its proximity to one of the edges, the potential barrier for such a process would be greatly reduced. However, I argued that such a model would fail to produce the appropriate periodicity. According to the London theory results of Kogan, Clem and Mints for thin rings in the limit of vanishing magnetization, the period in the free-energy is given by

$$H_0 = 2\phi_0 \frac{\ln(b/a)}{\pi(b^2 - a^2)} \quad (5.11)$$

as discussed in the previous section. The period in the magnetoresistance oscillations matches this period because the vortices must pass between the inner radius,  $a$  and the outer radius,  $b$ . If vortices were passing between the outer radius and a defect situated at a radius of  $b - \delta$ , the period in magnetoresistance oscillations should be similar to

$$H_0^{\text{defect}} = 2\phi_0 \frac{\ln(b/b - \delta)}{\pi(b^2 - (b - \delta)^2)} \approx \frac{\phi_0}{\pi b^2}. \quad (5.12)$$

In addition, if vortices were passing to defects near the edges of the sample, the fitted values of the ring's width,  $w_m^{\text{fit}}$ , would be expected to be  $\sim \delta$ . This was not seen.

These findings support the idea that surface scattering leads to an increase in the effective penetration depth, lowering the potential barrier faced by vortices attempting to pass through the ring. This effect is particularly prominent in Sr<sub>2</sub>RuO<sub>4</sub>, making it a difficult material to work with and even more difficult to perform theoretical predictions of sample behavior. Ab initio style calculations are nearly impossible because the magnitude of the gap can vary wildly in regions in which the crystal structure appears regular to the naked eye. Even producing micron-sized samples which undergo a superconducting transition is a difficult task.

# 6 Vortex Induced Phase Shifts

In this chapter I want to explore the consequences of vortices trapped in the bulk of a superconducting ring. First, consider the potential barrier given by Kogan, Clem, and Mints for a vortex to pass into a small, superconducting ring: equation (5.9). Explicitly, this is

$$V_{in}^+(N, H, v) = \epsilon_v(v) + \epsilon_0 \left\{ \left[ 2N + \frac{\ln(b/v)}{\ln(b/a)} \right] \frac{\ln(b/v)}{\ln(b/a)} - 2h \frac{b^2 - v^2}{b^2 - a^2} \right\}. \quad (6.1)$$

This potential is plotted in figure 6.1 for two cases. On the left is the potential barrier for a ring with inner radius of 75 nm, outer radius of 100 nm, thickness 10 nm, with a penetration depth of 200 nm. From top to bottom, the lines represent the potential barriers with applied fields of  $h = 0, 10, 20, 30, 40$ , and 50. On the right are the potential barriers for a ring with the same parameters except for the inner and outer radii of 62.5 nm and 100 nm, respectively. From top to bottom, the lines represent the potential barrier with applied fields of  $h = 0, 10, 20, 30, 35$ , and 40. For the wider ring on the right, the highlighted

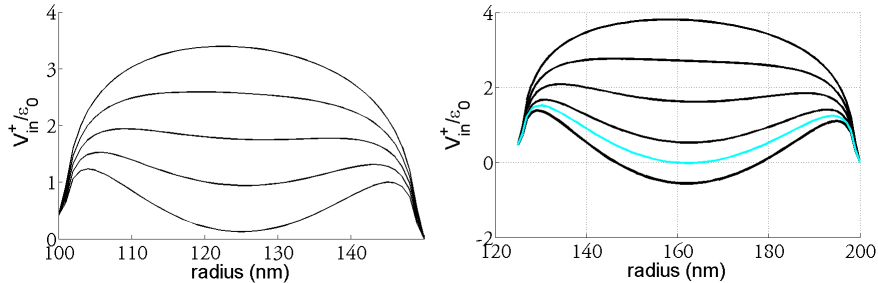


Figure 6.1: Plots of the potential barriers at various applied fields for two different ring widths.

potential barrier reaches zero for an applied field of  $h = 35$ . This is the field at which it is energetically favorable for a vortex to penetrate the sample,  $H_{c1}$ , and we should expect to see trapped vortices in the sample for applied fields greater than this value.

Now take a closer examination of the free-energy in equation (5.4). In the absense of vortices, this expression reduces to

$$\mathcal{F}(N, H) = \epsilon_0(N^2 - 2Nh + h^2\chi). \quad (6.2)$$

Equating  $\mathcal{F}(N, H)$  to  $\mathcal{F}(N + 1, H)$ , we find they are equal at the applied field of  $h = N + 1/2$ . Since  $\mathcal{F}(N - 1, H) = \mathcal{F}(N, H)$  at  $h = N - 1/2$ , we see that the period is  $\Delta h = 1$ .

Now suppose a vortex enters the sample. Equating  $\mathcal{F}(N, v, H)$  to  $\mathcal{F}(N + 1, v, H)$ , the transition is seen to happen at

$$h = (N + 1/2) + \frac{\ln(b/v)}{\ln(b/a)}. \quad (6.3)$$

Similarly, the transition between the  $N - 1$  and  $N$  states occurs at

$$h = (N - 1/2) + \frac{\ln(b/v)}{\ln(b/a)}. \quad (6.4)$$

The period hasn't changed but the oscillations have picked up a phase of  $\delta_v = \ln(b/v)/\ln(b/a)$ . The free energy for the thin ring with and without a vortex penetrating the ring is plotted in figure 6.2, illustrating this phase shift.

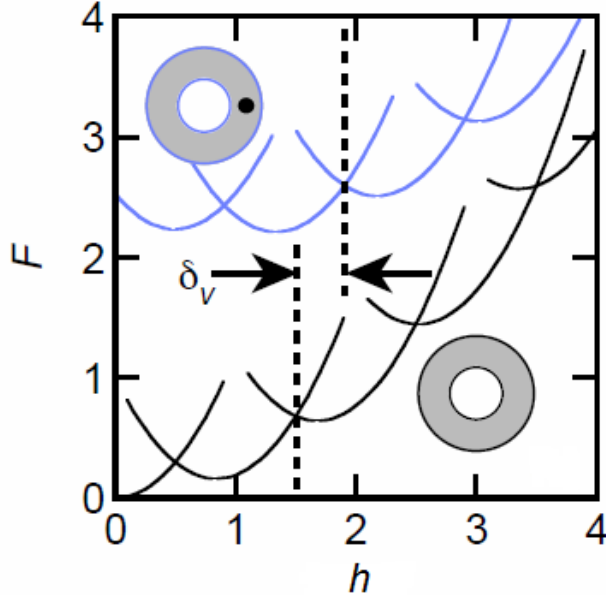


Figure 6.2: Plot of the free energy of fluxoid states with and without an Abrikosov vortex penetrating the ring.

Mills, Shen, Xu, and Liu have recently published measurements of magnetoresistance oscillations in the anisotropic superconductor NbSe<sub>2</sub> which seem to show phase shifts consistent with the presence of Abrikosov vortices in the ring[16].

The Ginzburg-Landau parameters of NbSe<sub>2</sub> have been inferred from measurements of its specific heat in high magnetic fields by Sanchez, et. al. [37] and measurements of the magnetic susceptibility by Banerjee, et. al. [38]. Their

	$\xi_{\parallel}$	$\xi_{\perp}$	$\lambda_{\parallel}$	$\lambda_{\perp}$	$\kappa_{\parallel}$	$\kappa_{\perp}$
Sanchez et. al.	10	3	200	202	21	72
Banerjee et. al.	8	3	107	455	14	49

Table 6.1: Measured Ginzburg-Landau parameters of  $\text{NbSe}_2$ . The length scales are given in nanometers.

results are summarized in table 6.1. Their conclusions are inconsistent with one another. I mention this only to highlight one of the difficulties in performing detailed calculations of vortex energetics.

A combination of electron-beam lithography and  $\text{CF}_4$  reactive ion plasma etching was used to prepare square, mesoscopic loops from single crystals of  $\text{NbSe}_2$ , as reported in [39]. Figures 6.4(a) and 6.4(b) show SEM images of the two loops. The thickness of both loops is  $\approx 10 \text{ nm}$ . Mills et. al. report that the loop in figure 6.4(a) has a median diameter  $r = 155 \pm 4 \text{ nm}$  and width  $w = 35 \pm 4 \text{ nm}$  while the loop of figure 6.4(b) has a median diameter of  $r = 200 \pm 4 \text{ nm}$  and width  $w = 70 \pm 4 \text{ nm}$ . The constrictions in the second sample have a width of  $\approx 35 \text{ nm}$  and are intended to reduce the potential barrier for vortex crossing to a similar value as that for the thinner ring.

The measured resistance oscillations of the two rings are displayed in figures 6.4(c) and 6.4(d). As with the resistance oscillations in  $\text{Sr}_2\text{RuO}_4$  discussed in the previous section, the magnitude of these oscillations are too great to be explained by the Little-Parks effect and are believed to be caused by vortices crossing the ring. The peaks in the data show where the ring's equilibrium fluxoid winding number changes. The first peak to the right of  $\mu_0 H = 0$  is where the equilibrium fluxoid winding number changes from  $n = 0$  to  $n = 1$ , the second peak where it changes from  $n = 1$  to  $n = 2$ , etc. Looking at 6.4(d), the space between the peaks, or the periodicity of the ring's free energy, is 840 Oe. Near the 5th peak, there is a phase shift of  $0.3\Delta H \approx 160 \text{ Oe}$ .

I undertook a numerical study of the ring displayed in 6.4(b). Using COMSOL, I solved the full Maxwell-Ginzburg-Landau equations (2.2) and (2.3) assuming a geometry reported by Mills, et. al. with the exception of the constrictions. This is shown in figure 6.3. I did not believe that the energetic stability of the Abrikosov vortices would be appreciably affected by their absence. For the purposes of the study, I assumed  $\lambda_{\parallel} = 200 \text{ nm}$ ,  $\xi_{\parallel} = 10 \text{ nm}$ , and that the anisotropy parameter,  $\gamma$ , was equal to 3.5. The results of that analysis are shown in figure 6.5. The bottom three curves are the free energy of the  $n = 6$ ,  $n = 7$ , and  $n = 8$  fluxoid state. The two curves in the upper right of the plot are the  $n = 7$  and  $n = 8$  fluxoid states with an Abrikosov vortex piercing the ring. The free energy of these states were calculated by simply giving the order-parameter the initial conditions of  $\psi = \exp[in\phi] \exp[in\arctan(y/(x-v))]$  where  $\phi$  is the azimuthal angle around the ring and  $v$  is the location of the vortex placed on the  $x$ -axis.

The period that I calculate is 0.054 T, in good agreement with the experi-

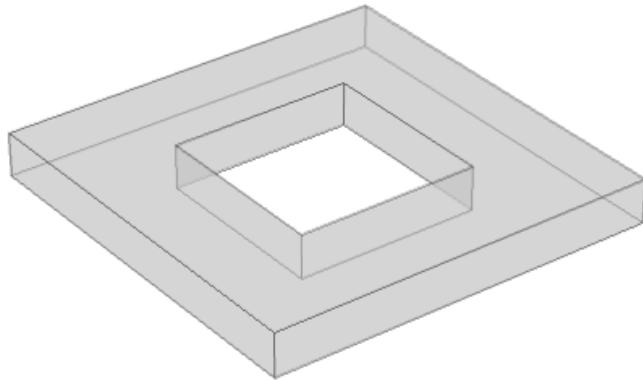


Figure 6.3: CAD drawing of Sample 1 sans-constrictions.

ment. The phase shift that I calculate is 260 Oe, higher than that found in the experiment. Also, in the experiment, the phase shift was seen to happen near the 5th peak in the resistance oscillations, or  $\mu_0 H \approx 0.25$  T. In my calculations, the fluxoid states with Abrikosov vortices present are not energetically stable, even at fields as high as 0.45 T.

There are a number of possible explanations for these discrepancies. Since the period closely matches that of the experimental sample, it is likely that the geometry and Ginzburg-Landau parameters are approximately correct. However, while I do not believe that the energetic stability of the Abrikosov vortices will be appreciably affected by a proper modeling of the constrictions, the magnitude of the phase shift may be very sensitive to geometric details.

A phenomenon that was not modeled by my calculations and which certainly will lower  $H_{c1}$  and make the presence of Abrikosov vortices more favorable is the effect of the currents passing through the ring. The currents will apply a Lorentz force on the vortices oriented in the  $z$ -direction, pulling the vortices into the ring. Mills et. al. include a study of this effect summarized in figure 6.6. Useful discussions of this effect, mostly in the context of nanowires, can be found in [40] and references therein. In addition, Berdiyorov, et. al. have demonstrated a method of modelling current activated vortices in finite-element-method calculations [41].

Another question to be answered is what the phase shift of subsequent vortices might be. Useful answers may even be found analytically. The conformal mapping procedure used by Kogan, Clem, and Mints, [42, Part II, Chap. 10], may be readily extended to a thin disk with a circumference forming any regular polygon and any number of evenly spaced Abrikosov vortices penetrating the ring. It is also a simple matter to perform finite-element calculations with multiple vortex entry using the already discussed techniques.

Vortex induced phase shifts could potentially be a robust means of detecting individual vortices and provide a new tool for studying vortex dynamics.

Unfortunately, at the present time, the demand for the study of the effects of geometry and the presence of current on Abrikosov vortex-induced phase shifts is lacking.

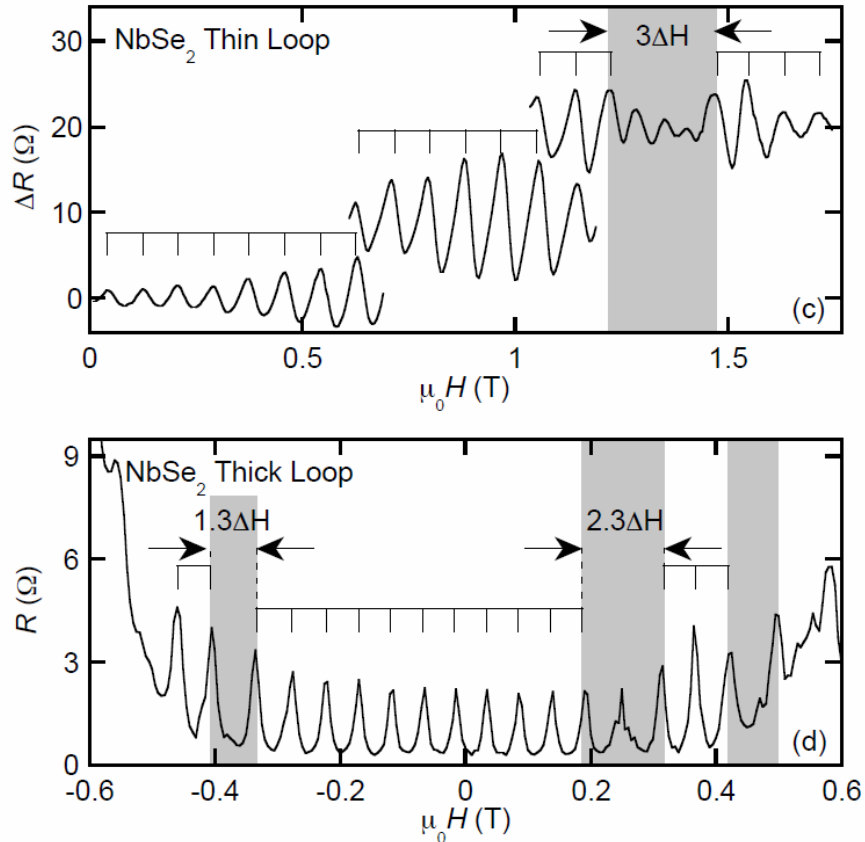
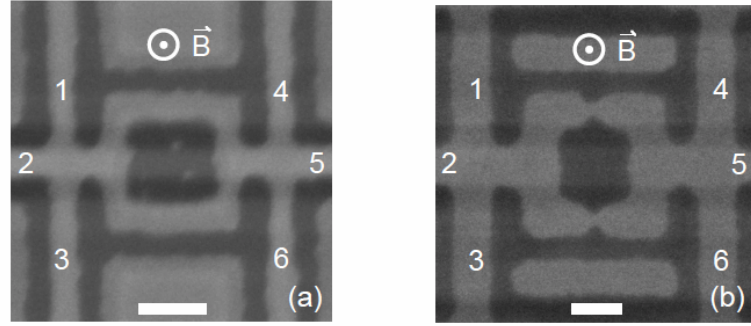


Figure 6.4: (a) SEM image of single-crystal  $\text{NbSe}_2$  loop with median diameter  $r \approx 160$  nm and width  $w \approx 35$  nm. For measurements, the current is sourced from 1 to 6 and voltage is measured from 3 to 4. Scale bar is 100 nm. (b) SEM image of  $\text{NbSe}_2$  loop with  $r \approx 200$  nm and width  $w \approx 70$  nm. The constricted regions have width  $\approx 30$  nm. Here the current is sourced from 1 to 5 and voltage is measured from 3 to 6. Scale bar is 100 nm. (c) Magnetoresistance of loop in (a) at 4.2, 3.8, and 1.8 K (bottom to top) and 500 nA after subtracting of a monotonic background and offsetting curves for clarity. Vertical lines are separated by  $H_0 = 840$  Oe. Shaded region denotes where phase shift occurs. (d) Magnetoresistance of loop in (b) at 1.8 K and 650 nA. Vertical lines are separated by  $H_0 = 540$  Oe, except where indicated. Shaded regions denote where phase shifts are acquired.

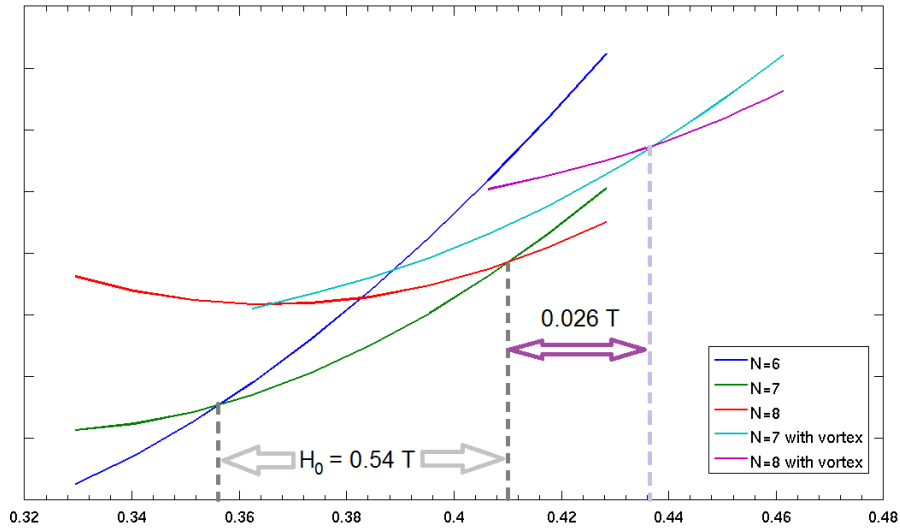


Figure 6.5: Plot of the free energy of fluxoid states with and without an Abrikosov vortex penetrating the ring.

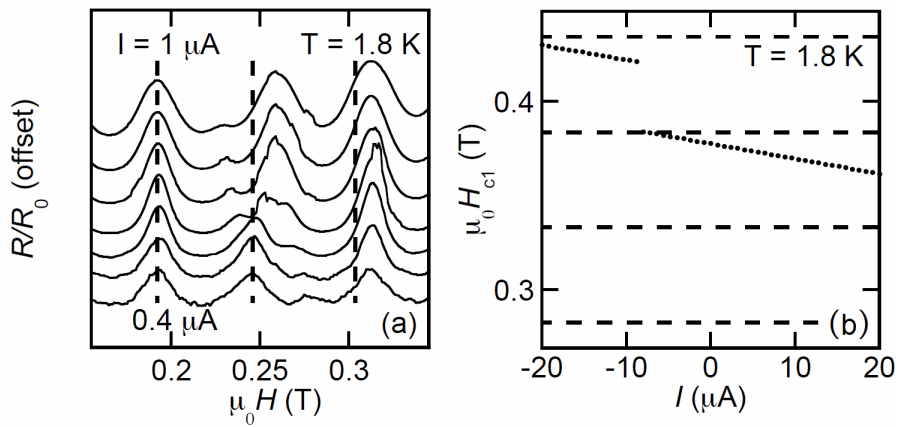


Figure 6.6: Figure (a) shows the measured resistance for various values of applied current. At higher applied currents the phase shift appears at lower applied magnetic fields. Figure (b) plots the field at which the Abrikosov vortex is presumed to enter versus applied current.

# 7 Conclusions

The model described in section II can qualitatively reproduce the results of the experiment described in [1]. Using kinematic spin polarization and a current coupling term in a two-component Ginzburg-Landau model, numerical results show that an in-plane field results in the increasing stability of a half-quantum vortex state. This leads to a wedge-like stability region in the half-flux state versus applied c-axis field as shown in Figure 4.2. Moreover, this is achieved using physically reasonable values of  $\mu$  and  $\rho_{sp}/\rho_s$ .

In comparing Figure 4.2 to Figure 1.2 there are some discrepancies that should be acknowledged. Firstly, the periodicity of the numerical result is approximately 30 Oe, while that of the data is 16 Oe. This is due to the fact that, assuming a penetration depth of 152 nm, the simulated ring's hole diameter is 0.6  $\mu\text{m}$  while the actual sample has a hole diameter of 0.75  $\mu\text{m}$ . A smaller hole necessitates a larger applied field in order to achieve the flux necessary to induce a fluxoid transition.

A more perplexing difference is in the magnitude of the moments, the numerical result's moments being an order of magnitude larger than those shown in Figure 1.2. These small magnetic moments seem to be found only in the smaller samples examined by Jang, et. al. The moment data collected from larger samples, as in Figure 2 of [2], seems to be of the appropriate order of magnitude. This phenomenon was also seen in the experiments of Cai, et. al. [4]. In Chapter 5, I suggested that this effect may be due to a suppression of the order-parameter due to surface scattering in samples that have dimension of  $\sim \xi$ . A thorough, quantitative understanding of this phenomenon is the most difficult problem presented in this thesis and I believe that to go beyond what I have explored here will require methods beyond Ginzburg-Landau theory.

While the origin of the suppressed magnetic moments may be qualitatively understood, this discrepancy in the magnitudes makes the interpretation of the experiments in [1] difficult. One possible scenario explaining the half-height jumps in magnetization were Abrikosov vortices piercing the side-wall nearly half-way between the top and bottom of the ring. One of the arguments against this is that the magnitude of the induced spin magnetic moment  $\mu_{HI}$  is an order of magnitude less than that produced by a side-wall vortex. The estimates of  $\mu_{HI}$  were determined by Jang, et. al. by using the formula  $\mu_{HI} = \delta H_z \Delta \mu_z / 4(H_x - H_{x,min})$  where  $\Delta \mu_z$  is the jump in magnetic moment upon entry of a unit vortex,  $\delta H_z$  is the width of the stability wedge,

and  $H_x - H_{x,min}$  is the amount of applied in-plane field over the minimum necessary to see half-flux states. For the data shown in Figure 1.2, the implied  $\mu_{HI} \approx 9 \times 10^{-15}$  emu while, from Figure 4.3,  $\mu_{HI} \approx 3.5 \times 10^{-14}$  emu. Since the measured  $\Delta\mu_z$  and  $\mu_{HI}$  appear to be poorly understood, this argument loses some credibility. However, the numerically calculated results shown in figure 4.2 and figure 4.3 show  $\mu_{HI}$  to be an order-of-magnitude smaller than  $\Delta\mu_z$ , suggesting that this is a generic feature. A better understanding will require an understanding of the character and stability of wall-vortex states. While I showed that it is difficult to find stable wall vortex states, a systematic approach to disproving them is lacking.

Finally, in Chapter 7, I presented an unfinished study of phase shift in the magnetoresistance oscillations of Type II superconductors. Using analytic London-limit expressions and numerical solutions, I showed that vortices trapped in multiply connected samples will cause phase shifts in free energy oscillations. I also suggested several directions a future study might readily take and which I would be interested in seeing as I believe the reward would outweigh the cost of such a study.

# A Magnetization curves of ring-shaped superconductors

Consider a long, thin-walled cylinder of radius  $R$  whose central axis is coincident with  $z$ -axis. In this limit, we may consider the magnitude of the order-parameter,  $|\psi|$ , and the supercurrent,  $\mathbf{J}$ , to be uniform throughout the cylinder. We also suppose that there is no appreciable magnetization so that  $\nabla \times \mathbf{A} = \mathbf{B}_{\text{ext}}$  throughout. Using equations (2.1) and (2.23), we can write the free energy density as

$$\begin{aligned} f &= \frac{1}{2}m|\mathbf{v}_s|^2 + \alpha|\psi|^2 + \frac{1}{2}\beta|\psi|^4 \\ &= \frac{\hbar^2}{2m}|\psi|^2 \left( \nabla\theta - \frac{2e}{\hbar}\mathbf{A} \right)^2 + \alpha|\psi|^2 + \frac{1}{2}\beta|\psi|^4. \end{aligned} \quad (\text{A.1})$$

Given the azimuthal symmetry of the geometry, we can take  $\nabla\phi = (2\pi n/2\pi R)\hat{\phi} = (n/R)\hat{\phi}$ . Choosing the gauge for the vector potential such that  $\mathbf{A} = (rB_{\text{ext}}/2)\hat{\phi}$  and rearranging, we can finally cast the free energy density in the form

$$f = \frac{\hbar^2}{2mR^2}|\psi|^2 \left[ \left( n - \frac{\Phi}{\Phi_0} \right)^2 + \alpha + \frac{1}{2}\beta|\psi|^2 \right] \quad (\text{A.2})$$

where  $\Phi$  is the flux threading the cylinder,  $2\pi RB_{\text{ext}}$ . Let us further assume that the externally applied field is of insufficient magnitude to suppress  $|\psi|^2$  to any appreciable extent. We may then drop the last two terms in the above equation. The resulting free energy as a function of the applied flux is plotted in figure A.1 for various values of  $n$ . At zero applied field, the system is in equilibrium with a winding number of  $n = 0$ , corresponding to zero field penetrating the ring. As the field is increased, the current and free energy increase until  $\Phi/\Phi_0$  exceeds  $1/2$ , where it becomes energetically favorable to transition to the  $n = 1$  state. This is accomplished by a vortex entering the cylinder, carrying quantum of flux, and increasing the winding number by one.

Keeping in mind that the cylinder will maintain a winding number closest to  $\Phi/\Phi_0$ , we can find the magnetization by taking the derivative  $M = -\partial F/\partial B_{\text{ext}}$ , shown in figure A.2.

Magnetization curves of cylinder or ring-shaped superconductors such as this simple example and those of figures 1.1 and 1.2 can generally be parameterized by their period,  $\Delta H$ , the slope of the curve, the magnetic susceptibility,  $\chi_M$ , and the magnitude of the discontinuity when the system transitions from one

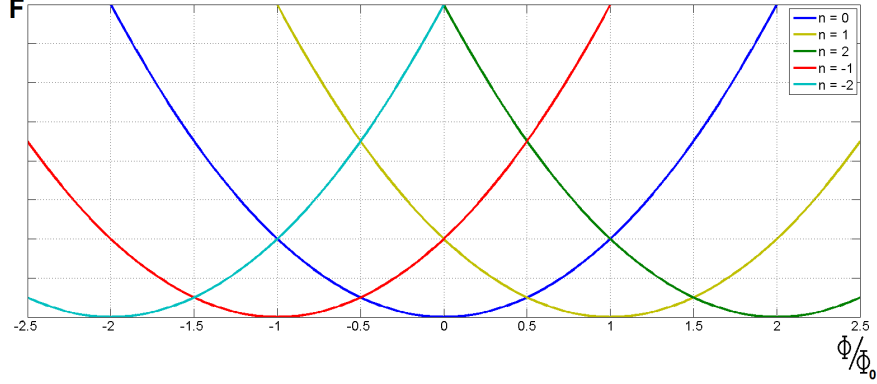


Figure A.1: The free energy of a thin-walled cylinder for various values of the winding number of the order parameter.

fluxoid state to another,  $\Delta M$ . In the case of the the thin-walled cylinder,

$$\Delta H = \Phi_0, \quad (\text{A.3})$$

$$\chi_M = \frac{\pi \hbar^2 R^2}{4e^2 \mu_0 \lambda^2}, \quad (\text{A.4})$$

and

$$\Delta M = \frac{\hbar^2}{4e^2 \mu_0 \lambda^2 R^2}. \quad (\text{A.5})$$

Analytic solutions exist for the case of an infinitely long cylinder such as those of Arutunian and Zharkov [43]. However, to derive useful formulae for the parameters of magnetization curves, the London limit, where one ignores variations in  $|\psi|$ , is normally taken. For the case of an infinitely long cylinder (length  $L \gg$  radius) with inner radius  $R_1$  and outer radius  $R_2$  in the London limit, Vakaryuk [24] gives

$$\Delta H = \frac{\Phi_0}{\pi R_1^2} \frac{a_{13}}{b_{12} - 2\lambda^2/R_1^2}, \quad (\text{A.6})$$

$$4\pi L^{-1} \chi_M = \frac{\pi R_3^2}{a_{13}} \left( b_{21} - \frac{4\lambda^4}{R_1^2 R_2^2} \frac{1}{b_{12}} \right), \quad (\text{A.7})$$

and

$$\Delta M = \frac{\Phi_0 L}{2} \left( 1 - \frac{2\lambda^2}{R_1^2 b_{12}} \right) \quad (\text{A.8})$$

where

$$\begin{aligned} a_{jk} &= K_0(j)I_0(k) - I_0(j)K_0(k) \\ b_{jk} &= K_2(j)I_0(k) - I_2(j)K_0(k) \end{aligned} \quad (\text{A.9})$$

and  $I_n$  and  $K_n$  are modified Bessel functions of  $n$ -th order and  $K_0(j) \equiv K_0(R_j/\lambda)$ , etc.

Other useful formulae are found by examining the London-limit solutions of thin (thickness  $d$ ), small (diameter  $\ll \Lambda = \lambda^2/2d$ ) superconducting rings given

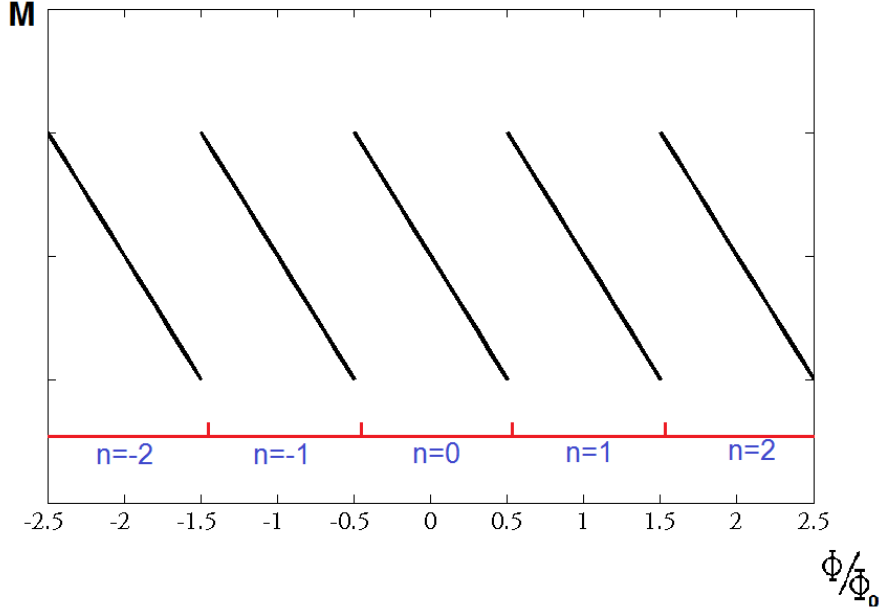


Figure A.2: The magnetic moment of a long, thin-walled cylinder.

by [17]. Analysis of those solutions gives

$$\Delta H = \frac{2\Phi_0 \ln(R_2/R_1)}{\pi(R_2^2 - R_1^2)}, \quad (\text{A.10})$$

$$\chi_M = 2\epsilon_0 \frac{R_2^2/R_1^2 + 1}{R_2^2/R_1^2 - 1} \ln(R_2/R_1), \quad (\text{A.11})$$

and

$$\Delta M = \frac{\Phi_0(R_2^2 - R_1^2)d}{16\pi\lambda^2} \quad (\text{A.12})$$

where  $\epsilon_0$  is an energy scale given by  $\Phi_0^2/8\pi^2\Lambda$ .

For real geometries, one must resort to numerical methods as I have done in this thesis, but these solutions provide insight, intuition, approximations, and sanity checks on numerical solutions.

Now consider a two component model with a current-current coupling. In section 2.2 I showed that, in the London-limit, we have the effective free energy

$$f = |\psi|^2 \frac{\hbar^2}{2m^*} \left\{ 2(1+b) \left| \nabla \chi - \frac{2e}{\hbar} \mathbf{A} \right|^2 + 2(1-b) |\nabla \phi|^2 \right\} \quad (\text{A.13})$$

or

$$f = \rho_s \left| \nabla \chi - \frac{2e}{\hbar} \mathbf{A} \right|^2 + \rho_{\text{spin}} |\nabla \phi|^2 \quad (\text{A.14})$$

where  $\chi$  may possess a half-integer winding number. In order for this free energy density to be stable,  $\rho_{\text{spin}}$  must not be negative. We can examine this free energy in the case of a very thin cylinder of radius  $R$  as we did for the single component

free energy and write

$$f = \frac{\rho_s}{R^2} \left( n - \frac{\Phi}{\Phi_0} \right)^2 + \rho_{\text{spin}} |\nabla \phi|^2 \quad (\text{A.15})$$

where  $n$  is allowed to be an integer or half-integer and  $\rho_{\text{spin}} |\nabla \phi|^2$  is a geometry-dependent energy cost only present when  $n$  is a half-integer. For a generic value of  $\rho_{\text{spin}}$  the free energy of various winding numbers is plotted in figure A.3. By increasing the current-current coupling parameter,  $b$ , we can lower  $\rho_{\text{spin}}$  and make the half-flux states more stable. This is the mechanism by which I can change the minimum in-plane field required to see half-flux states in my calculations.

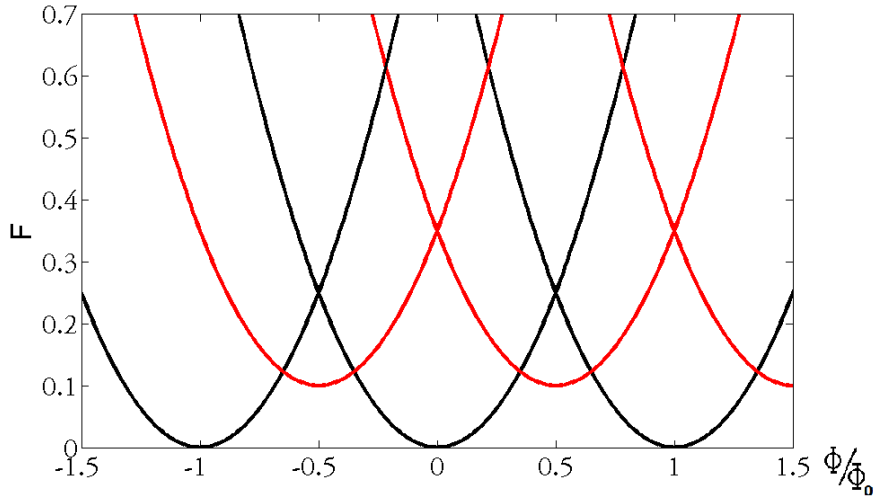


Figure A.3: The free energy curves of a two component system with current-current coupling. The states with half-integer flux winding are shown in red.

# B Magnetic moment curves of rings with weak links

I began by looking at thin superconducting rings with Josephson junctions. The basic shape was a ring with an outer radius of  $3.5 \lambda_{\parallel}$  and an inner radius of  $2.5 \lambda_{\parallel}$ , making the ring thickness  $1 \lambda_{\parallel}$ . The height of the ring was made to be  $1.8 \lambda_{\parallel}$ . Here  $\lambda_{\parallel}$  refers to the ab-plane penetration depth. Meano et.al. lists its value at 0K to be 152 nm[11].

The first type of Josephson junction was created by subtracting two toroids from the azimuthally symmetric ring making a bow-tie shaped junction (Fig. B.1). In this study, we set  $\text{sgn}(\alpha)=-1$  in the volume of the ring, and  $\text{sgn}(\alpha)=+1$  in the surrounding vaccuum, as if there were a superconducting region embedded in a normal metal. This led to areas outside of the defined ring boundaries to have a non-zero value for the order parameter. It becomes difficult, then, to model a given experimental geometry because the volume in which  $\text{sgn}(\alpha)=-1$  does not correspond to the real, physical sample volume. In this case, in order to weaken the superconductivity at the bow-tie shaped junction to an extent at which it behaved in the manner of a weak-link Josephson junction, it was necessary to place an actual gap in the junction. There is a region with  $\text{sgn}(\alpha)=+1$  in the middle of the junction. Various gap lengths were tested to obtain behavior similar to the experimental magnetization.

Figure B.4 is a plot of the z-component of the magnetization versus the field strength in the z-direction for various junction widths given in nanometers. This was obtained by establishing a superconducting phase at 0 Gauss (G) and then increasing the field strength to 65 G as slowly as was reasonable given finite time constraints. This was done in order to minimize effects of hysteresis due to increasing the field strength too quickly, a phenomenon we have dubbed “computational hysteresis”. This sort of hysteresis can be seen most clearly by examining the magnetization curve for a junction length of 0nm; in other words, a solid ring. The curve plotted is smooth, whereas the theoretical curve giving the equilibrium magnetization exhibits jump discontinuities.

The order-of-magnitude of the magnetization is consistent with that found by Raffi Budakian et. al.[1]. The magnetic susceptibility of this ring is  $-1.5 \times 10^{-14} \text{cm}^3$  which is around twice as large as that found in the sample of [1]. The period of the magnetization curve is around 35 G which implies an effective radius, defined by  $r_{\text{eff}} = \sqrt{\Phi_0/2\pi B_{\text{ext}}}$ , of  $2.8 \lambda_{\parallel}$ . One can also see that the magnetization curve becomes more sinusoidal and the non-diamagnetic shifts in the magnetization decrease as the Josephson coupling is decreased. All of these

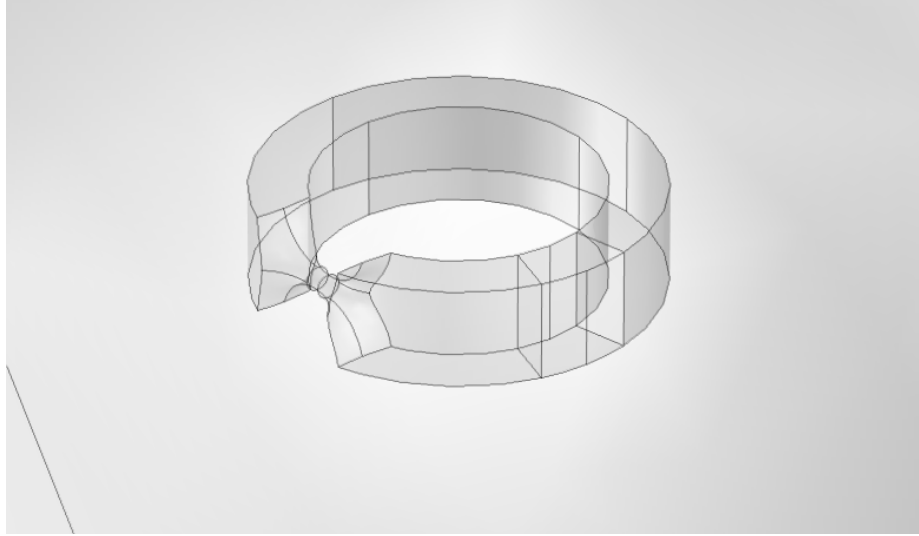


Figure B.1: Thin ring Josephson junction with cylindrical symmetry.

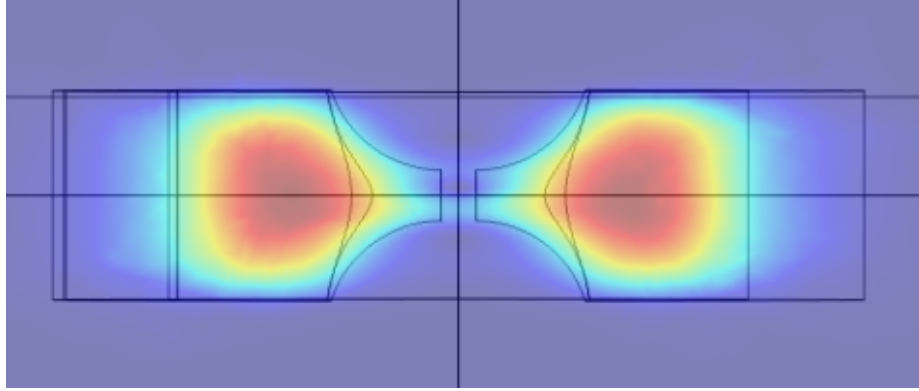


Figure B.2: Magnitude of the order parameter in junction with vortex.

results are consistent with the expected behavior of rings of this type and thus the simulations are believed to be reliable.

I decided to continue examinations using the 46 nm long junction. I performed tests in which a superconducting state was established in zero magnetic field. A magnetic field oriented in the +x-direction was slowly turned up to a desired value. At that point, a magnetic field in the z-direction was applied and slowly turned from 0 to 65 G. Figure B.5 is a plot of the z-component of the magnetization as a function of the c-axis field strength for various values of the in-plane field. Figure B.6 is the same plot where I have attempted to subtract the Meissner slope and offset the curves.

With the use of COMSOL, one can examine the solutions of the order parameter using integrated plotting software. Doing this, one can see that vortices pass through the junction oriented along the x-axis. Figure B.2 is a temperature plot of the magnitude of the order parameter showing a vortex in the junction. The vortex shown occurred in the field sweep with 800 G of in-plane field and

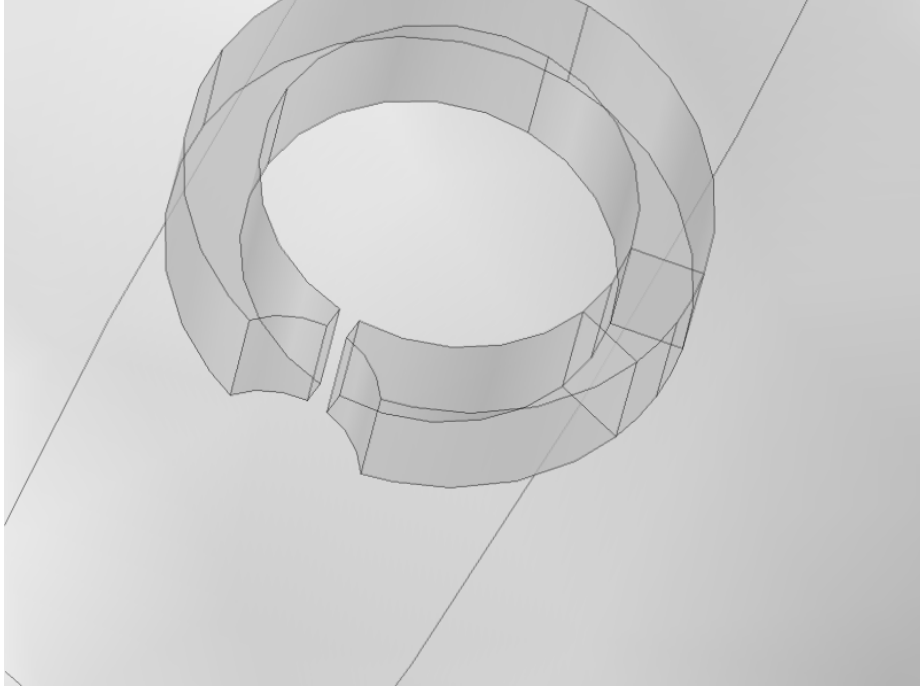


Figure B.3: Thin ring Josephson junction pinched in one direction.

shows the asymmetric character of vortices aligned in the ab-plane of  $\text{Sr}_2\text{RuO}_4$ . At lower values of in-plane field the vortices passing through the junction are not kinked to as great of a degree.

What this shows, though, is that vortices passing through the junction in this way fail to effect the critical current of the ring and the sinusoidal shape of the magnetization curve is maintained.

In the second junction geometry tested, the ring was only pinched in the x-direction, leaving the height of the ring unchanged in the weak link region (Fig. B.3). We once again ran tests with a 46 nm wide gap of normal metal in the junction. Significant differences with the first junction type were noticed. Figure B.7 shows vortices entering the junction due to the application of an increasing magnetic field in the  $x$ -direction. These vortices were not seen in the first type of junction, presumably because the junction simply wasn't big enough. Two vortices entering symmetrically from the top and bottom, as shown, is expected due to the reflection symmetry in the sample and hence, no magnetization in the  $z$ -direction is seen. Similar results were seen when this symmetry was broken by creating an asymmetric junction that was wider at the bottom than at the top. Geometrical asymmetry must be present to create only a single vortex in the junction as this would imply a non-zero magnetization in the  $z$ -direction. Once again, these vortices do not exit the back of the ring but bend and exit toward the plus and minus  $z$ -directions. A vortex does not penetrate the backside of the ring until the in-plane field value is over 800 G.

Figure B.8 shows the magnetization curves of this ring with various values

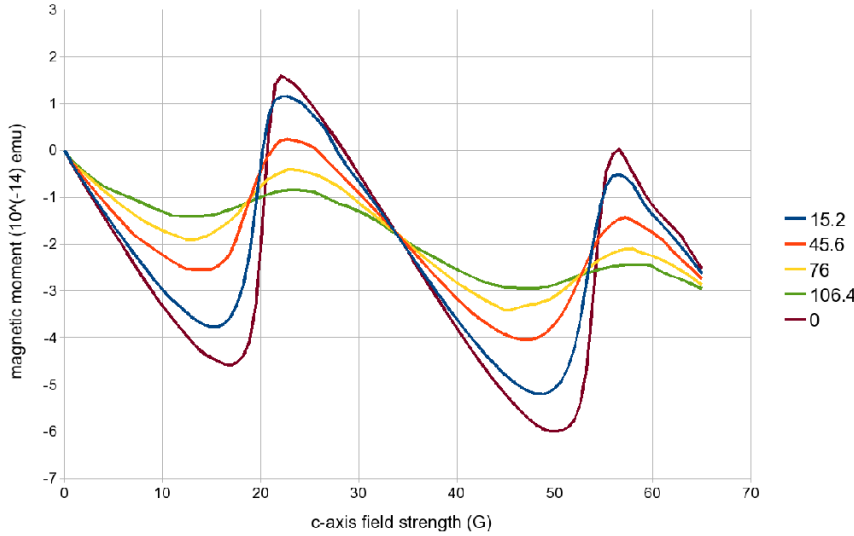


Figure B.4: Magnetization curves of a thin ring with a Josephson junction of varying coupling strengths.

of in-plane field, the Meissner slopes subtracted off and the curves offset. One can see that the curve with 300 G of in-plane field appears to have a double bump in the magnetization during the first transition similar to what was found in the data. The cause of this effect, as evidenced by animations of the order parameter in the junction, is that the vortices passing through the junction spend more time in the middle of the junction than near the edges. When the vortex stops in the middle of the junction the magnetization curve remains a constant (neglecting the diamagnetic Meissner response) until it starts moving again, leading to this double-step pattern. However, it doesn't appear to be periodic as it doesn't occur in the same way in the second transition. Moreover, this effect disappears when the in-plane field is turned up to 500 G. Here we see the expected sinusoidal behavior but with a phase shift. The 800 G curve shows a severe depression of the critical current.

To examine this behavior further we ran the same simulations but with the in-plane field turned by 30 degrees. Figure B.9 shows the simulated data over the range -65 G to 65 G. Once again, the 300 G magnetization curve shows a modulation of the critical current during the first transition. However, this time the curve doesn't show “stepping” but rather two “bumps” at the same value. This effect is, once again, not periodic and vanishes when the in-plane field is increased.

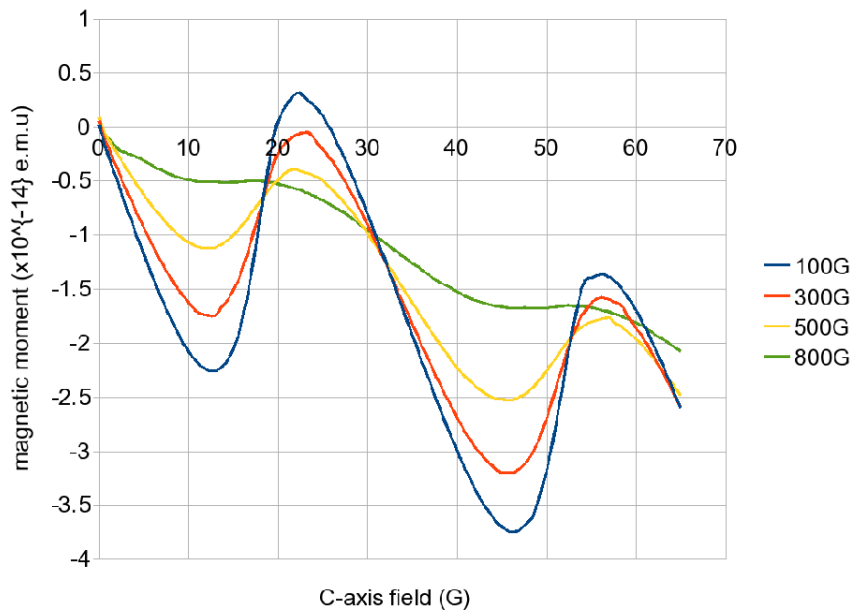


Figure B.5: Magnetization curves of 46 nm junction with in-plane field.

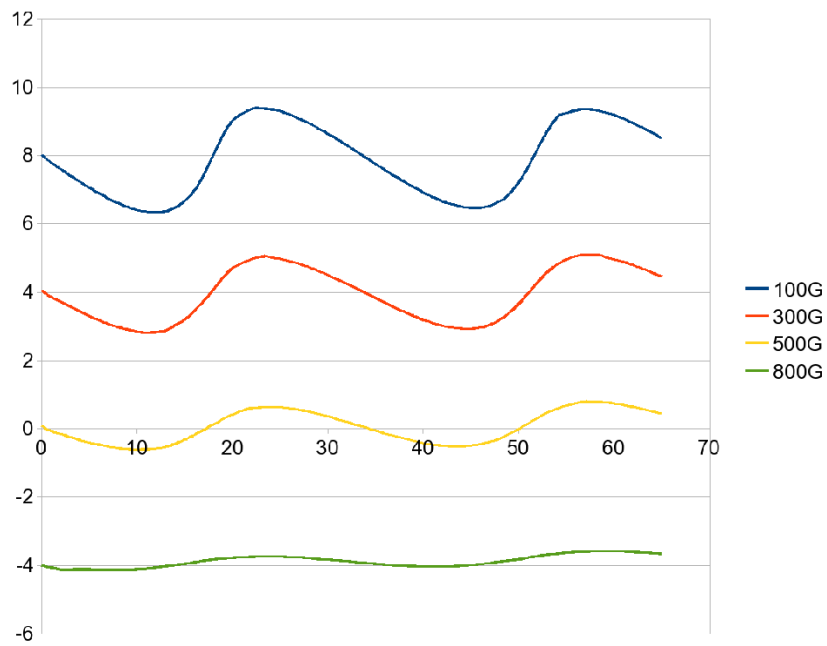


Figure B.6: Magnetization curves of 46 nm junction with Meissner slope subtracted and curves offset

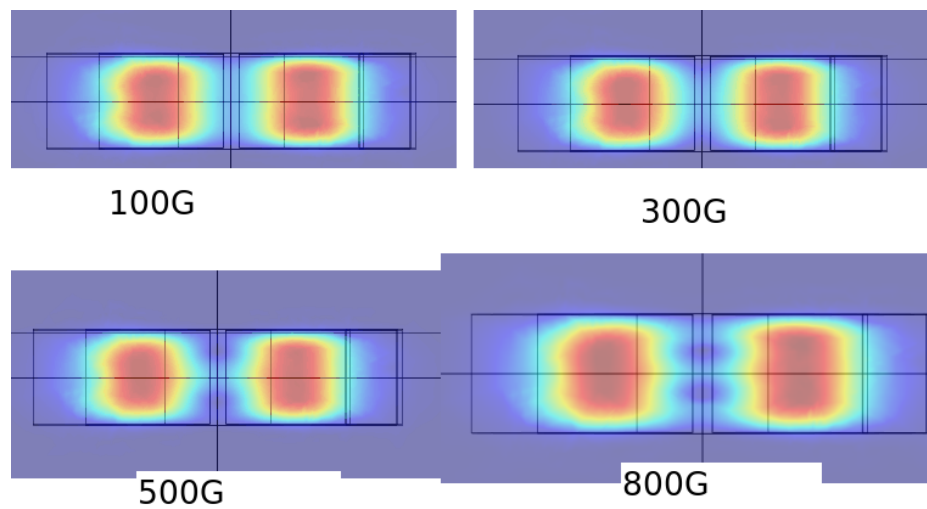


Figure B.7: Vortices in second geometry.

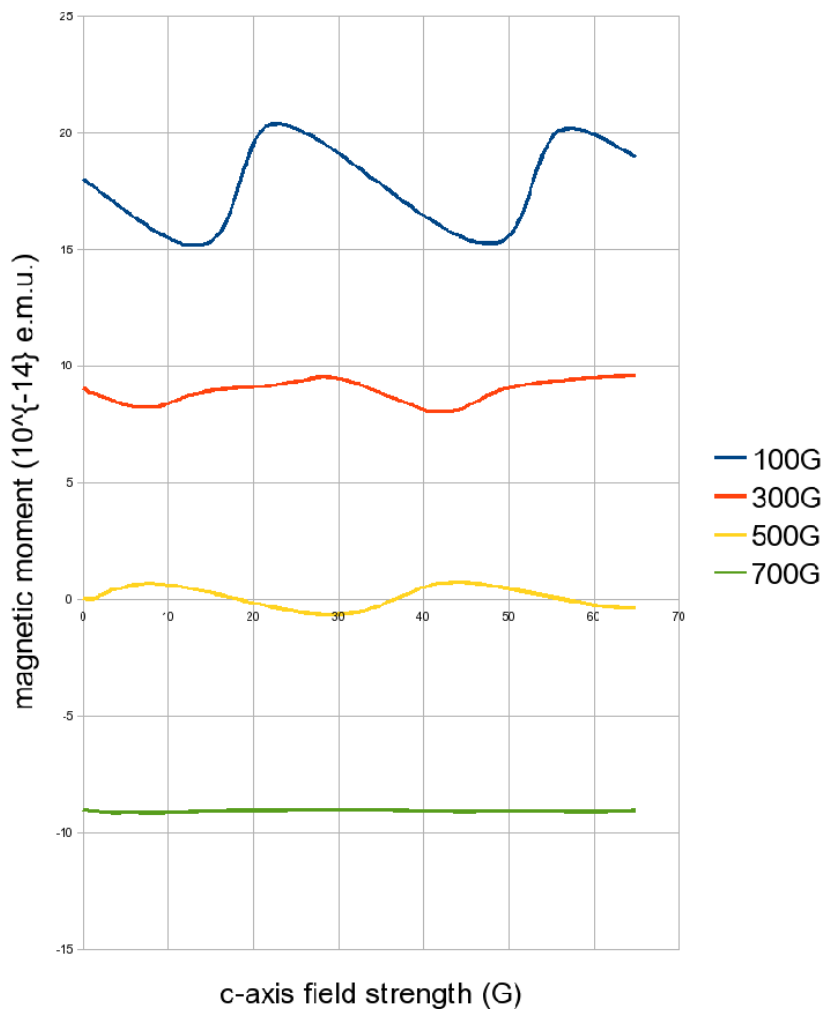


Figure B.8: Magnetization curves of second ring.

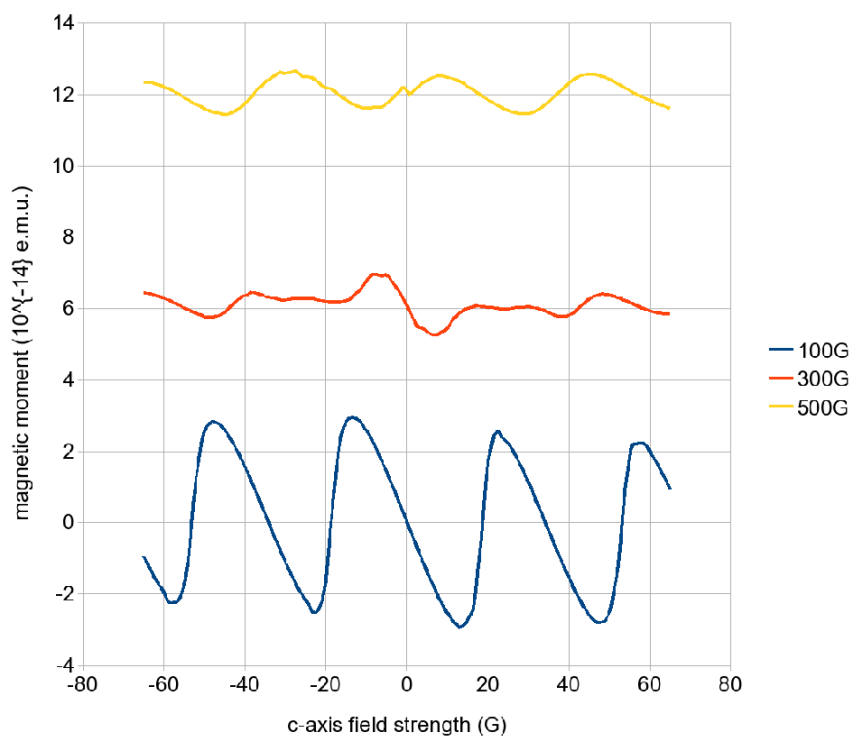


Figure B.9: Second ring with in-plane field rotated by 30 degrees.

# C Magnetic field delocalization and flux inversion

Babaev, et. al. have reported in [5] solutions for the asymptotic behavior of the magnetic field near a vortex core in a generalized two-component Ginzburg-Landau model. They find that only in exceptional cases is the magnetic field screened exponentially at long distances and that near the center of the vortex, the magnetic field actually changes directions, a phenomenon that has been dubbed w-modulation. I will briefly summarize their argument here.

They consider a free energy of the form

$$E = \frac{1}{2} \int dx dy \left\{ |(\partial_k + ieA_k)\psi_1|^2 + |(\partial_k + ieA_k)\psi_2|^2 + \eta_1(u_1^2 - |\psi_1|^2)^2 + \eta_2(u_2^2 - |\psi_2|^2)^2 + (\epsilon_{ij}\partial_i A_j)^2 \right\}. \quad (\text{C.1})$$

Neglecting anisotropy, this is analogous to the model free energy of section 2.5 without the current-current coupling described in section 2.2. I can write the pseudopotential terms of our half-quantum vortex model as

$$V(\psi_\uparrow, \psi_\downarrow) = \sum_{\uparrow, \downarrow} \left\{ (\alpha \mp g\mu_B|B_\parallel|)|\psi_i|^2 + \frac{1}{2}\beta|\psi_i|^4 \right\} \quad (\text{C.2})$$

which shows that  $2\eta_i$  corresponds to  $\alpha \mp g\mu_B|B_\parallel|$  while  $\eta_i u_i$  corresponds to  $\beta/2$ . This free energy yields the equations of motion

$$(\partial_k + ieA_k)^2\psi_1 + 2\eta_1(u_1^2 - |\psi_1|^2)\psi_1 = 0, \quad (\text{C.3})$$

$$(\partial_k + ieA_k)^2\psi_2 + 2\eta_2(u_2^2 - |\psi_2|^2)\psi_2 = 0, \quad (\text{C.4})$$

and

$$-\epsilon_{kj}\partial_j B = J_k \quad (\text{C.5})$$

where  $J_k = \frac{i}{2}e\{\psi_1(\partial_k - ieA_k)\psi_1^* + \psi_2(\partial_k - ieA_k)\psi_2^* + \text{c.c.}\}$ . They then seek solutions of the form

$$(A_1, A_2) = \frac{a(r)}{r}(-\sin\theta, \cos\theta); \quad \psi_i = \rho_i e^{-in_i\theta}, \quad (\text{C.6})$$

enforcing an integer winding number of the order parameters about the vortex situated at the origin. They also require that  $J_k \rightarrow 0$  and  $\rho_i \rightarrow u_i$  as  $r \rightarrow \infty$ , ensuring a localized solution. Performing the line integral of  $|\mathbf{J}|$  around a closed

path located far from the origin yields the flux quantization condition

$$a(r) \rightarrow \frac{1}{2}\Phi, \quad \text{where} \quad \Phi = \frac{n_1 u_1^2 + n_2 u_2^2}{u_1^2 + u_2^2}. \quad (\text{C.7})$$

An examination of this expression is illuminating. If the superfluid densities are the same,  $u_1 = u_2$ , then a half-flux vortex state can be obtained if  $n_1 \neq n_2$ . However, if  $u_1 \neq u_2$ , the state is no longer possesses a half-integer of flux. This is the case for our model outlined in Chapter 2 due to the kinematic-spin-polarization terms. Coupling to the in-plane magnetic field renders the two superfluid densities slightly unequal.

Substituting the ansatz (C.6) into the equations of motion gives the coupled ordinary differential equations

$$\rho_1'' + \frac{\rho_1'}{r} - \frac{(n_1 - ea)^2}{r^2} \rho_1 + 2\eta_1(u_1^2 - \rho_1^2)\rho_1 = 0, \quad (\text{C.8})$$

$$\rho_2'' + \frac{\rho_2'}{r} - \frac{(n_2 - ea)^2}{r^2} \rho_2 + 2\eta_2(u_2^2 - \rho_2^2)\rho_2 = 0, \quad (\text{C.9})$$

and

$$a'' - \frac{a'}{r} - e(ae(\rho_1^2 + \rho_2^2) - n_1\rho_1^2 - n_2\rho_2^2) = 0. \quad (\text{C.10})$$

Babaev et. al. then observe that in the fractional flux states in which  $n_1 \neq n_2$ , neither  $n_1 - ea$  or  $n_2 - ea$  approaches zero as  $r \rightarrow \infty$ . Therefore,  $\rho_1$  and  $\rho_2$  can not approach their equilibrium values of  $u_1$  and  $u_2$  exponentially fast. They make the self-consistent assumption that

$$\rho_i \sim u_i - \alpha_i r^{-2} \quad (\text{C.11})$$

at large  $r$  for some real coefficients  $\alpha_1$  and  $\alpha_2$ . Inserting into the differential equations and demanding that the leading term ( $O(r^{-2})$ ) vanish gives the result

$$\alpha_i = \frac{(n_i - \Phi)^2}{4\eta_i u_i}, \quad i = 1, 2. \quad (\text{C.12})$$

By a similar method, they assume that

$$a(r) \sim \frac{\Phi}{e} - \beta r^{-2} \quad (\text{C.13})$$

and find that

$$\beta = \frac{1}{2e(u_1^2 + u_2^2)} \left[ \frac{(n_1 - \Phi)^3}{\eta_1} + \frac{(n_2 - \Phi)^3}{\eta_2} \right] \quad (\text{C.14})$$

Quoting Babaev, et. al. :

"Now  $B = r^{-1}a'(r)$ , so in the case where  $\Phi > 0$ ,  $a(r)$  interpolates between  $a(0) = 0$  and  $a_\infty > 0$ , so one expects  $a'(r) > 0$  uniformly, and hence  $B(r) > 0$ . In particular, one expects  $a(r)$  to approach its boundary value  $a_\infty$  from below, so that  $\beta > 0$ . But in this regard, this formula contains a surprise: it is quite

possible for  $\beta$  to be negative. In this case, since  $B(r) \sim 2\beta r^{-4}$  at large  $r$ , we see that the magnetic field has to flip its direction as one travels out from the vortex core: it is positive for small  $r$  and negative for large  $r$ .”

They then show that this is not a pathological case and is true for half the  $(u_i, \eta_i)$  parameter space. Figure C.1 shows numerical solutions of the behavior of the superfluid density near a vortex core for various flux fractions. Notice the characteristic “W” shape of the component without a flux winding. I report this here because I serendipitously discovered w-modulation in my own numerical studies. Figure C.2 shows superfluid velocity profiles of  $\psi_\uparrow$  and  $\psi_\downarrow$  in the half-flux state in a ring geometry. Notice the upturn in the velocity of the component without a phase winding near the inner edge of the ring. This came as some surprise at first since we were initially intending to make exactly half-flux states. However, kinematic-spin-polarization produces a difference in magnitude between the two components leading to w-modulation.

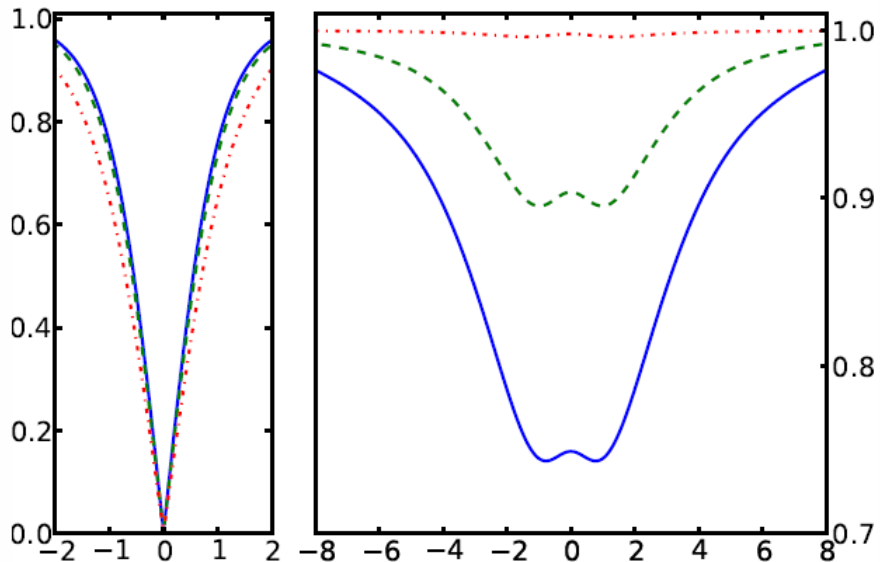


Figure C.1: From [5]. The behavior of the superfluid densities near the core of a vortex. On the left is plotted  $|\psi_1|$  with  $|\psi_2|$  on the right. The blue line represents a flux fraction of  $5/6$ , the green,  $5/7$ , and the red,  $1/3$ . the component with the phase winding is  $\psi_1$ . Notice the “W”-shape of the profile of  $\psi_2$ .

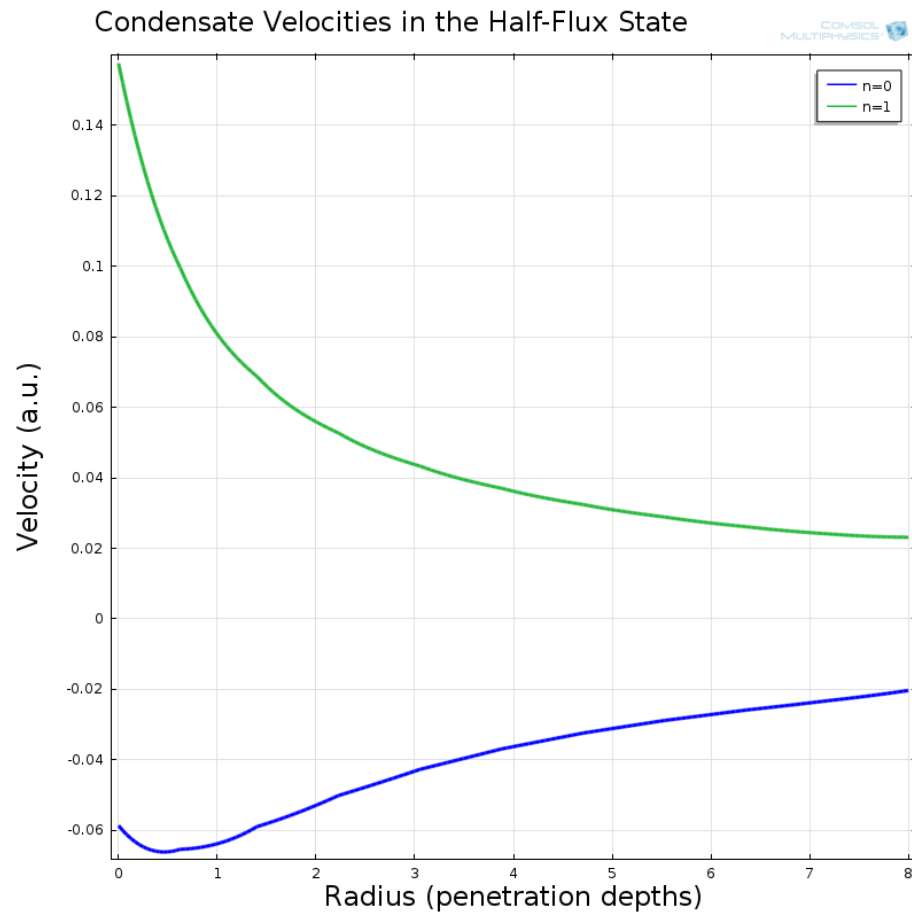


Figure C.2: Velocity profile of  $\psi_{\uparrow}$  and  $\psi_{\downarrow}$  in the half-flux state in a ring geometry. Contrary to integer flux states, the superfluid velocity of the component without a flux winding increases near the vortex core.

# D A Brief Introduction to the Finite-Element-Method

In this appendix I wanted to give a flavor of what the finite-element-method is about and hopefully illustrate why it has become the de facto method for solving partial differential equations in asymmetric geometries. Given space and time constraints, I think the most illuminating method of beginning is with a simple example.

Consider Poisson's equation

$$\nabla^2 u(x, y) = f(x, y) \quad \text{in } \Omega \quad (\text{D.1})$$

subject to the Dirichlet boundary condition

$$u = 0 \quad \text{on } \partial\Omega \quad (\text{D.2})$$

where  $\Omega$  is a connected open region in the  $(x, y)$  plane whose boundary  $\partial\Omega$  is a smooth manifold. The first step in solving this problem via the finite-element-method is to convert it to its *weak formulation*.

## D.1 Weak formulation

First, let's write our differential equation as

$$\nabla \cdot \nabla u(x, y) = f(x, y) \quad \text{in } \Omega. \quad (\text{D.3})$$

Now let  $v$  be an arbitrary, *nice* function on  $\Omega$ , which satisfies  $v = 0$  on  $\partial\Omega$ . This will be called the *test function*. Multiply our differential equation by  $v$  and integrate over  $\Omega$ :

$$\int_{\Omega} v \nabla \cdot \nabla u \, dx dy = \int_{\Omega} v f \, dx dy \quad (\text{D.4})$$

Now use Gauss's theorem to integrate by parts:

$$\int_{\partial\Omega} v \nabla u \cdot \mathbf{n} \, ds - \int_{\Omega} \nabla v \cdot \nabla u \, dx dy = \int_{\Omega} v f \, dx dy \quad (\text{D.5})$$

Utilizing the boundary condition on  $v$ , this reduces to

$$\int_{\Omega} v f \, dx dy = - \int_{\Omega} \nabla v \cdot \nabla u \, dx dy \equiv -\phi(u, v). \quad (\text{D.6})$$

In the general case the boundary term may not vanish. This is the so-called weak formulation. Reversing the steps, it is easy to see that if  $u$  satisfies the weak form, it will satisfy the original differential equation. However, notice that it only requires that  $u$  be once differentiable as opposed to the original problem. This is why it is called weak. It is possible to find solutions to the weak formulation of a problem for which the original form has no meaning.

$\phi$  can be turned into an inner product on a space  $H_0^1(\Omega)$  of once differentiable functions on  $\Omega$  that are zero on  $\partial\Omega$ . This is known as a *Sobolev space*.

The next step in utilizing the finite-element-method is to discretize the problem.

## D.2 Discretization

The general idea is to turn our infinite-dimensional problem in equation (D.6) into a finite-dimensional version. We do this by discretizing  $\Omega$ , a process known as creating a “mesh”, and defining a finite, linearly-independent set of test functions on each element of the discretized space. An example of a mesh on a two-dimensional disk is shown in figure D.1. There are many complex algorithms for creating a mesh for a general geometry. Most popular finite-element software packages have several and are, in large part, what give these software packages their value.

To better understand this step in the process it is easier to briefly look at a simpler problem in one-dimension. Imagine you wanted to solve Poisson’s equation on the line segment  $(0, 1)$ . First you would divide the line interval  $(0, 1)$  into as many segments as you’d like by *node points*:  $x_1, x_2$ , etc., creating the mesh. Once we have a mesh, we can introduce our approximation to  $u$ . We want to be able to describe  $u$  with a finite number of parameters, or *degrees of freedom*. We will then insert this approximation into the weak form of our differential equation, generating a system of linear equations.

To start with, let’s divide the interval into two equal parts:  $0 < x < 1/2$  and  $1/2 < x < 1$ . Our node point, then, is  $x = 1/2$ . We will approximate  $u$  by linear functions on each segment, meaning that to completely characterize the solution, we only need to know  $u(x)$  at  $x = 0, x = 1/2$ , and  $x = 1$ . Denote these values as  $U_1, U_2$ , and  $U_3$ , respectively. These are the degrees of freedom.

Now, we can write

$$u(x) = U_1 w_1(x) + U_2 w_2(x) + U_3 w_3(x) \quad (\text{D.7})$$

where  $w_i$  are piecewise linear functions such that on each mesh interval, it equals 1 at the  $i^{th}$  node point, and equals 0 at the other node points. For example,  $w_1(x) = 1 - x$  if  $0 \leq x \leq 1/2$  and 0 if  $1/2 \leq x \leq 1$ . These are called the basis functions or *shape functions*. The set of functions  $u(x)$  so constructed is called a *finite element space*.

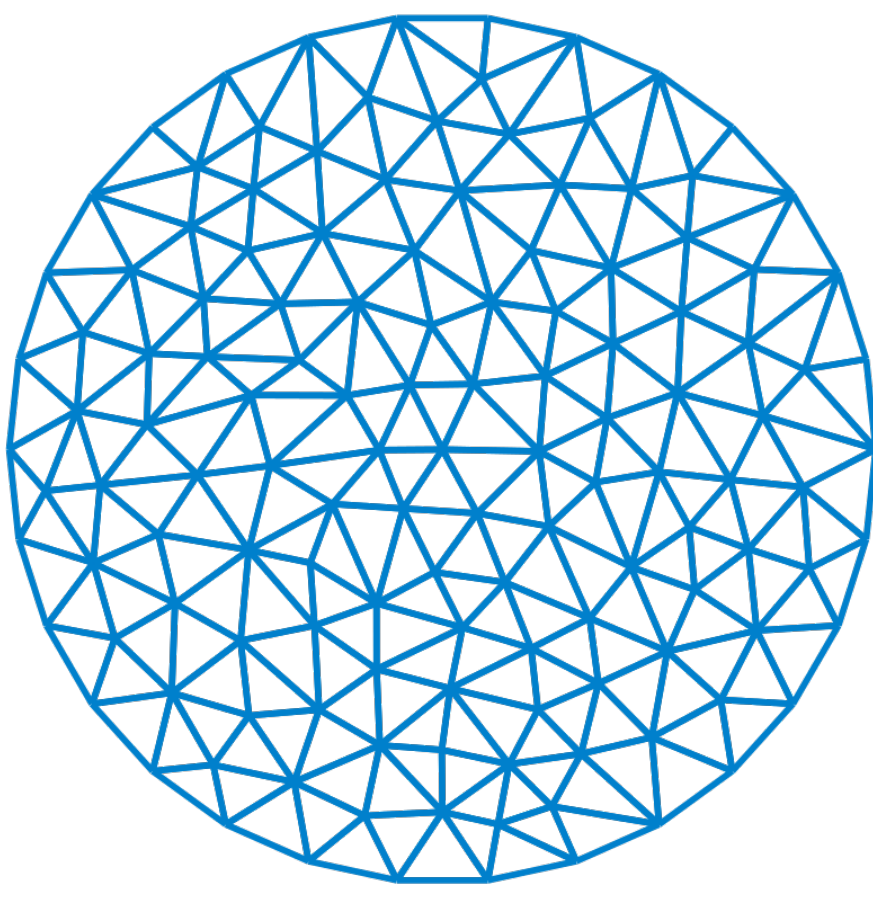


Figure D.1: The mesh of a two-dimensional disk by triangles. ("Finite element triangulation" by Oleg Alexandrov - self-made, with en:Matlab. Licensed under Public Domain via Wikimedia Commons)

For the triangulated mesh of our two-dimensional problem we must first define local coordinates on each mesh element. COMSOL defines local coordinates  $\xi_1, \xi_2$  in each triangle such that  $\xi_1 \geq 0, \xi_2 \geq 0, \xi_1 + \xi_2 \leq 1$ . The shape functions are then given in table D.1.

The primary advantage of this choice of basis is that the inner products

$$\langle w_i, w_j \rangle = \int_0^1 w_i w_j dx \quad (\text{D.8})$$

Node Point	Shape Function
(0,0)	$1 - \xi_1 - \xi_2$
(1,0)	$\xi_1$
(0,1)	$\xi_2$

Table D.1: Linear shape functions for triangular mesh elements.

and

$$\phi(w_i, w_j) = \int_0^1 w'_i w'_j dx \quad (\text{D.9})$$

will be zero for almost all  $i, j$ . In the one-dimensional case, the support of  $w_k$  is the interval  $[x_{k-1}, x_{k+1}]$ . Hence,  $\langle w_i, w_j \rangle$  and  $\phi(w_i, w_j)$  vanish whenever  $|j - k| > 1$ .

For the two-dimensional case, if  $x_i$  and  $x_j$  do not share an edge of the triangulation mesh, then

$$\int_{\Omega} w_i w_j dx dy \quad (\text{D.10})$$

and

$$\int_{\Omega} \nabla w_i \cdot \nabla w_j dx dy \quad (\text{D.11})$$

both vanish.

To cast the one-dimensional problem in matrix form for a general number of mesh elements, write

$$u(x) = \sum_{k=1}^n U_k w_k(x) \quad (\text{D.12})$$

and

$$f(x) = \sum_{k=1}^n F_k w_k(x). \quad (\text{D.13})$$

Then, taking  $v(x)$  in equation (D.6) to be  $w_i(x)$  for  $i = 1, \dots, n$ , we have

$$-\sum_{k=1}^n U_k \phi(w_i, w_j) = \sum_{k=1}^n F_k \int_0^1 w_i w_j dx \quad \text{for } j = 1, 2, \dots, n. \quad (\text{D.14})$$

Now let  $\mathbf{U} = (U_1, U_2, \dots, U_n)^T$ ,  $\mathbf{F} = (F_1, \dots, F_n)^T$  as well as

$$L_{ij} = \phi(w_i, w_j) \quad (\text{D.15})$$

and

$$M_{ij} = \int_0^1 w_i w_j dx. \quad (\text{D.16})$$

Equation (D.6) may be restated as

$$-\mathbf{L}\mathbf{U} = \mathbf{MF}. \quad (\text{D.17})$$

Most of the entries of  $L$  and  $M$  are zero because the basis functions  $w_i$  only have support on a small part of the mesh. We now have a system of  $n$  linear equations where the matrix that we need to invert,  $L$ , consists mostly of zeros. There are many solvers for inverting such *sparse* matrices. The steps needed to produce this matrix equation in higher dimensions are exactly the same.

The great strength in this method lies in its ability to handle complicated geometries. In finite *difference* methods, it is difficult to work with a compu-

tational grid that isn't rectangular. In the finite-element-method, on the other hand, can discretize the geometry in a variety of ways. The finite elements discussed here are called *Lagrange elements* of order 1. The order refers to the fact that the basis elements were first order polynomials. A Lagrange element of order  $k$  uses shape functions which are  $k$ -th order polynomials. Notice that the Lagrange elements of order 1 would not be solutions of the original differential equation, which requires  $u(x)$  to be twice differentiable.

There are many ways of discretizing a geometry and there are many different types of shape functions that one can utilize. The *COMSOL Multiphysics Reference Guide*[44] is a wealth of information of this type. For general information about the finite-element-method, I found useful the textbook *The Finite Element Method: Basic Concepts and Applications*[45], by Darrel W. Pepper and Juan C. Heinrich.

# References

- [1] J. Jang, D. G. Ferguson, V. Vakaryuk, R. Budakian, S. B. Chung, P. M. Goldbart, and Y. Maeno. Observation of half-height magnetization steps in  $\text{Sr}_2\text{RuO}_4$ . *Science*, 331:186–188, January 2011.
- [2] Joonho Jang, Raffi Budakian, and Yoshiteru Maeno. Phase-locked cantilever magnetometry. *App. Phys. Lett.*, 98, 2011.
- [3] W. A. Little and R. D. Parks. Observation of quantum periodicity in the transition temperature of a superconducting cylinder. *Phys. Rev. Lett.*, 9:9–12, Jul 1962.
- [4] X. Cai, Y. A. Ying, N. E. Staley, Y. Xin, D. Fobes, T. J. Liu, Z. Q. Mao, and Y. Liu. Unconventional quantum oscillations in mesoscopic rings of spin-triplet superconductor  $\text{Sr}_2\text{RuO}_4$ . *Phys. Rev. B*, 87:081104, Feb 2013.
- [5] Egor Babaev, Juha Jäykkä, and Martin Speight. Magnetic field delocalization and flux inversion in fractional vortices in two-component superconductors. *Phys. Rev. Lett.*, 103:237002, Dec 2009.
- [6] D. A. Ivanov. Non-abelian statistics of half-quantum vortices in  $p$ -wave superconductors. *Phys. Rev. Lett.*, 86:268–271, Jan 2001.
- [7] Ady Stern, Felix von Oppen, and Eros Mariani. Geometric phases and quantum entanglement as building blocks for non-abelian quasiparticle statistics. *Phys. Rev. B*, 70:205338, Nov 2004.
- [8] Michael Stone and Suk-Bum Chung. Fusion rules and vortices in  $p_x + ip_y$  superconductors. *Phys. Rev. B*, 73:014505, Jan 2006.
- [9] G.M. Luke, Y. Fudamoto, K.M. Kojima, M.I. Larkin, J. Merrin, B. Nachumi, Y.J. Uemura, Y. Maeno, Z.Q. Mao, Y. Mori, H. Nakamura, and M. Sigrist. Time-reversal symmetry-breaking superconductivity in  $\text{sr}_2\text{ruo}_4$ . *Nature*, 394:558–561, Aug 1998.
- [10] P. G. Kealey, T. M. Riseman, E. M. Forgan, L. M. Galvin, A. P. Mackenzie, S. L. Lee, D. McK. Paul, R. Cubitt, D. F. Agterberg, R. Heeb, Z. Q. Mao, and Y. Maeno. Reconstruction from small-angle neutron scattering measurements of the real space magnetic field distribution in the mixed state of  $\text{sr}_2\text{ruo}_4$ . *Phys. Rev. Lett.*, 84:6094–6097, Jun 2000.
- [11] Andrew Peter Mackenzie and Yoshiteru Maeno. The superconductivity of  $\text{Sr}_2\text{RuO}_4$  and the physics of spin-triplet pairing. *Rev. Mod. Phys.*, 75:657–712, May 2003.
- [12] Kevin Roberts, Raffi Budakian, and Michael Stone. Numerical study of the stability regions for half-quantum vortices in superconducting  $\text{sr}_2\text{ruo}_4$ . *Phys. Rev. B*, 88:094503, Sep 2013.

- [13] Suk Bum Chung, Hendrik Bluhm, and Eun-Ah Kim. Stability of half-quantum vortices in  $p_x + ip_y$  superconductors. *Phys. Rev. Lett.*, 99:197002, Nov 2007.
- [14] Victor Vakaryuk and Anthony J. Leggett. Spin polarization of half-quantum vortex in systems with equal spin pairing. *Phys. Rev. Lett.*, 103:057003, Jul 2009.
- [15] I. Sochnikov, A. Shaulov, Y. Yeshurun, G. Logvenov, and I. Božović. Oscillatory magnetoresistance in nanopatterned superconducting  $\text{La}_{1.84}\text{Sr}_{0.16}\text{CuO}_4$  films. *Phys. Rev. B*, 82:094513, Sep 2010.
- [16] Shaun A Mills, Chenyi Shen, Zhuan Xu, and Ying Liu. Detection of individual abrikosov vortices in  $\text{NbSe}_2$  loops by quantum oscillations. *arXiv preprint arXiv:1410.8469*, 2014.
- [17] V. G. Kogan, John R. Clem, and R. G. Mints. Properties of mesoscopic superconducting thin-film rings: London approach. *Phys. Rev. B*, 69:064516, Feb 2004.
- [18] Michael Tinkham. *Introduction to Superconductivity: Second Edition*. McGraw-Hill Book Co., New York, 1996.
- [19] Michael Stone and Paul Goldbart. *Mathematics for Physics*. Cambridge University Press, 2009.
- [20] R. Balian and N. R. Werthamer. Superconductivity with pairs in a relative  $p$  wave. *Phys. Rev.*, 131:1553–1564, Aug 1963.
- [21] Manfred Sigrist and Kazuo Ueda. Phenomenological theory of unconventional superconductivity. *Rev. Mod. Phys.*, 63:239–311, Apr 1991.
- [22] D. Völlhardt and P. Wolfle. *The Superfluid Phases of Helium 3*. Taylor & Francis, 1990.
- [23] G.E. Volovik. *Exotic Properties of Superfluid  $^3\text{He}$* . World Scientific, 1992.
- [24] Victor Vakaryuk. Stability of topological defects in chiral superconductors: London theory. *Phys. Rev. B*, 84:214524, Dec 2011.
- [25] E. Kanda, editor. *Proc. 12th Int. Conf. Low Temp. Phys.* Kyoto, 1970.
- [26] S. Jonathan Chapman, Qiang Du, and Max D. Gunzburger. On the lawrence-doniach and anisotropic ginzburg-landau models for layered superconductors. *SIAM J. Appl. Math.*, 55:156–174, 1995.
- [27] William D. Gropp, Hans G. Kaper, Gary K. Leaf, David M. Levine, Mario Palumbo, and Valerii M. Vinokur. Numerical simulation of vortex dynamics in type-ii superconductors. *Journal of Computational Physics*, 123(2):254 – 266, 1996.
- [28] Wei Jiang and Qinglin Tang. Numerical study of quantized vortex interaction in complex ginzburglandau equation on bounded domains. *Applied Mathematics and Computation*, 222(0):210 – 230, 2013.
- [29] Sylvia Serfaty. Ginzburglandau vortices, coulomb gases, and abrikosov lattices. *Comptes Rendus Physique*, 15(6):539 – 546, 2014.

- [30] David Ferguson. *Explorations of Domain Walls and Half-Quantum Vortices in Unconventional Superconductors*. PhD thesis, University of Illinois at Urbana-Champaign, 2011.
- [31] A. P. Mackenzie, R. K. W. Haselwimmer, A. W. Tyler, G. G. Lonzarich, Y. Mori, S. Nishizaki, and Y. Maeno. Extremely strong dependence of superconductivity on disorder in  $\text{sr}_2\text{ruo}_4$ . *Phys. Rev. Lett.*, 80:161–164, Jan 1998.
- [32] A. P. Mackenzie, R. K. W. Haselwimmer, A. W. Tyler, G. G. Lonzarich, Y. Mori, S. Nishizaki, and Y. Maeno. Erratum: Extremely strong dependence of superconductivity on disorder in  $\text{sr}_2\text{ruo}_4$  [phys. rev. lett. 80, 161 (1998)]. *Phys. Rev. Lett.*, 80:3890–3890, Apr 1998.
- [33] R. P. Groff and R. D. Parks. Fluxoid quantization and field-induced depairing in a hollow superconducting microcylinder. *Phys. Rev.*, 176:567–580, Dec 1968.
- [34] Ilya Sochnikov, Avner Shaulov, Yosef Yeshurun, Logvenov Gennady, and Ivan Božović. Large oscillations of the magnetoresistance in nanopatterned high-temperature superconducting films. *Nature Nanotechnology*, 5:516–519, 2010.
- [35] Vinay Ambegaokar and B. I. Halperin. Voltage due to thermal noise in the dc josephson effect. *Phys. Rev. Lett.*, 22:1364–1366, Jun 1969.
- [36] M. Tinkham. Resistive transition of high-temperature superconductors. *Phys. Rev. Lett.*, 61:1658–1661, Oct 1988.
- [37] D. Sanchez, A. Junod, J. Muller, H. Berger, and F. Lévy. Specific heat of  $2\text{h-nbse}_2$  in high magnetic fields. *Physica B*, 204:167–175, 1995.
- [38] S.S. Banerjee, N.G. Patil, K. Ghosh, Subir Saha, G.I. Menon, S. Ramakrishnan, A.K. Grover, P.K. Mishra, T.V. Chandrasekhar Rao, G. Ravikumar, V.C. Sahni, C.V. Tomy, G. Balakrishnan, D. Mek Paul, and S. Bhattacharya. Magnetic phase diagram of anisotropic superconductor  $2\text{h-nbse}_2$ . *Physica B*, 237-238:315–317, Jul 1997.
- [39] S. A. Mills, N. E. Staley, J. J. Wisser, C. Shen, Z. Xu, and Y. Liu. Single-crystal superconducting nanowires of  $\text{nbse}_2$  fabricated by reactive plasma etching. *App. Phys. Lett.*, 104:052604, 2014.
- [40] Alexey Bezryadin. *Superconductivity in Nanowires*. Wiley-VCH, November 2012.
- [41] G. R. Berdyyorov, M. V. Milošević, M. L. Latimer, Z. L. Xiao, W. K. Kwok, and F. M. Peeters. Large magnetoresistance oscillations in mesoscopic superconductors due to current-excited moving vortices. *Phys. Rev. Lett.*, 109:057004, Jul 2012.
- [42] P.M. Morse and H. Feshbach. *Methods of Theoretical Physics*. McGraw-Hill, 1953.
- [43] R.M. Arutunian and G.F. Zharkov. Behavior of a hollow superconducting cylinder in a magnetic field. *Journal of Low Temperature Physics*, 52(5-6):409–431, 1983.
- [44] COMSOL Multiphysics Reference Guide.

- [45] Darrel W. Pepper and Juan C. Heinrich. *The Finite Element Method: Basic Concepts and Applications*. Taylor & Francis Group, 2006.